Comparative Study of Small-Signal Stability under Weak AC System Integration for Different VSCs

Xiaojun Lu, Wang Xiang, *Member, IEEE*, Weixing Lin, *Member, IEEE*, Jinyu Wen, *Member, IEEE*

***Abstract*- Voltage source converters (VSCs) with self-commutation ability are suitable to interconnect weak AC systems. This paper conducts a comparative study of the small-signal stability characteristics for three typical VSCs, namely, the two-level VSCs (TL-VSCs), the half-bridge modular multilevel converters (HB-MMCs) and the hybrid MMCs (HY-MMCs), under weak AC system integration with special consideration on both inverter and rectifier operation. The frequency responses based on impedance models are compared using the frequency-domain analysis. The oscillation frequencies and mainly participated state variables of the unstable modes are compared using root locus and participation factor analysis in time-domain. Proper parameter retuning approaches for stability enhancement are proposed. The above analysis is adequately validated by electromagnetic simulations.**

***Index Terms*—Small-signal model, small-signal stability, modular multilevel converter, weak AC system, HVDC transmission.**

NOMENCLATURE

Acronyms

VSC	voltage source converter
MMC	modular multilevel converter
IGBT	insulated gate bipolar transistor
TL-VSC	two-level voltage source converter
HB-MMC	half-bridge modular multilevel converter
HY-MMC	hybrid modular multilevel converter
HBSM	half-bridge sub-module
FBSM	full-bridge sub-module
OHL	overhead line
SCR	short circuit ratio
ACC	AC current controller
DCC	DC current controller
CCSC	circulating current suppression controller
PLL	phase lock loop
PF	participation factor
PCC	point of common coupling
CCS	controlled current source
CVS	controlled voltage source

Subscripts

x, *y*	axis of the rotating frame synchronized with PCC voltage
d, *q*	axis of the rotating frame synchronized with the measured PCC voltage by PLL
pu	per unit
fil	filtered signals
ref	reference values

Variables

u_s	AC system voltage
P_{ac}	AC-side active power of converters
Q	reactive power of converters
u_{dc}	DC terminal voltage of VSCs
i_{dc}	DC terminal current of VSCs
i	AC-side current of VSCs
u_v	AC-side voltage of VSCs
u_p	PCC voltage
m	modulation signal of VSCs
m_p, m_n	modulation signals for upper and lower arm
i_{up}, i_{dn}	upper and lower arm current
u_{cp}^{Σ} , u_{cn}^{Σ}	the total capacitor voltage of the upper and lower arm
M_x,M_y/ M_d,M_q	fundamental-frequency modulation signal in *xy* / *dq* frame
M_{x2},M_{y2}/ M_{d2}, M_{q2}	second harmonic modulation signal in *xy* / *dq* frame
M_{dc}	DC modulation signal
u_{cx2}^{Σ} , u_{cy2}^{Σ}	second harmonic of u_{cp}^{Σ} in *xy* frame
u_{cx}^{Σ} , u_{cy}^{Σ}	fundamental-frequency part of u_{cp}^{Σ} in *xy* frame
u_{c0}^{Σ}	DC component of u_{cp}^{Σ}
$u_{c,avg}$	average capacitor voltage, equal to u_{c0}^{Σ}
u_{vx}, u_{vy}	u_v in *xy* frame
i_x, i_y / i_d, i_q	i in *xy* / *dq* frame
i_{diff}	circulating current
i_{diff0}	DC component of i_{diff}
i_{diffx2}, i_{diffy2}	second harmonic of i_{diff} in *xy* frame
x_P,x_Q,x_{Id},x_{Iq}	state variables in ACC outer and inner loop
x_{Pdc},x_{Idc}	state variables in DCC outer and inner loop

Parameters

R_s/L_s	equivalent AC system resistance/inductance
K_T	turn-ratio of the AC transformer
R_T/L_T	AC transformer resistance/inductance
C_{dc}	lumped capacitance of TL-VSC

[1] This work is sponsored by the Joint Funds of the National Natural Science Foundation of China (U1766211), the National Natural Science Foundation of China (51907068) and the Key Research and Development Program of Shaanxi (2017ZDXM-GY-135). (Corresponding author: *Wang Xiang*)

X. Lu, and J. Wen are with the State Key Laboratory of Advanced Electromagnetic Engineering and Technology, Huazhong University of Science and Technology, Wuhan 430074, China. (e-mail:luxiaojun1212@ foxmail.com, jinyu.wen @hust.edu.cn).

W. Xiang is with the Department of Electronic and Electrical Engineering, University of Strathclyde, Glasgow, G1 1XW, U.K. (e-mail: xiangwang1003@ foxmail.com).

W. Lin is with the TBEA SunOasis Co,. Ltd, Urumuchi 830011, Xinjiang, China. (e-mail: weixinglin@foxmail.com).

C_{sub}	capacitance of sub-modules in MMC
R_{arm}	equivalent resistance of MMC per arm
L_{arm}	Arm inductance of MMC
L_{ac}	AC inductance for TL-VSC
N_{sub}	total number of sub-modules in one MMC arm
K_{PO}/K_{PI}	proportional gain for ACC outer/inner loop
K_{IO}/K_{II}	integration gain for ACC outer/inner loop
L_{pu}	feedforward gain for AC current in ACC
K_{POdc}/K_{PIdc}	proportional gain for DCC outer/inner loop
K_{IOdc}/K_{IIdc}	integration gain for DCC outer/inner loop
K_{Udcs}	feed-forward gain of DC voltage
K_{Ppll}/K_{Ipll}	proportional and integration gain of PLL
K_{PC}/K_{IC}	proportional and integration gain for CCSC

I. Introduction

VSCs are self-commutated, which are suitable to interconnect renewable generation systems or other weak AC systems. Various topologies of VSCs have been applied in commercial applications, such as TL-VSCs [1], HB-MMCs [2] and HY-MMCs [3].

The TL-VSCs with IGBTs in series connection are adopted for integrating wind power or interconnecting asynchronous AC systems, with lumped DC capacitors installed at the DC-side to support the DC link voltage. Restricted by the capacity and voltage withstand ability, TL-VSCs are mainly adopted in applications with low DC voltage and power ratings [1]. Driven by the need for high-voltage bulk-power transmission, MMCs based on HBSMs are proposed in [2]. The distributed capacitors in SMs relieve the requirement for the simultaneous triggering of IGBTs, making it easier to construct high DC voltage transmission. However, both TL-VSCs and HB-MMCs are vulnerable to DC faults [4][5], limiting their application in OHL transmission systems. The HY-MMC is proposed in [3], with FBSMs and HBSMs mixed in the phase arms. The negative insertion of the FBSMs endows HY-MMC with the ability to control its DC output voltage independently of the AC voltage. By optimally designing the sub-module ratio and the active fault current control strategy, HY-MMC can ride through DC faults without interruption [6][7].

The self-commutation ability of VSCs makes them applicable to the weak AC grid connection. The grid-side converter for the wind power generation system normally adopts TL-VSCs, which are usually integrated through long-distance AC transmission lines with relatively large reactance, resulting in a weak AC system integration situation. Under such conditions, small-signal stability of TL-VSCs may be worsened because of the undesired interaction among different control units [8]-[10] or the negative resistance effect of the AC output impedance [12][13]. While for practical MMC projects, such as a ±350kV/ 1000MW back-to-back HVDC HB-MMC project [14], or a ±800kV hybrid three-terminal OHL-HVDC project employing HY-MMCs [15], the converter is normally connected to a strong AC system. But the SCR of the AC system can be varied due to the variation of the seasonal loads or the change of the grid structure by the scheduled maintenance or occasional AC faults. Therefore, MMCs may be forced to be connected with a weak AC system, which may cause small-signal stability problems under usual operation points and regular control modes, such as high-frequency oscillation in the AC voltage [14][15], or a wide-band oscillation in the transmitted power as reported in [16].

The above-mentioned instability has been separately researched employing the time-domain modal analysis or the frequency-domain impedance analysis [8]-[16]. However, the instability characteristic of these three topologies under weak AC system integration has not been adequately compared. The small-signal dynamics for the TL-VSCs and HB-MMCs are compared in [17], which shows that HB-MMCs produce more complex interaction patterns due to the internal dynamics. Nevertheless, for the stability issue under weak AC system integration, whether the internal dynamics of MMCs may affect the stability characteristics still needs to be investigated.

Existing publications mainly focus on one specific operation state for a single terminal VSC under constant AC voltage control mode. In practical MMC-HVDC projects, the reactive power control instead of the AC voltage is conventionally adopted. As mentioned before, the strength of the AC system may be suddenly weakened due to the tripping of AC transmission lines. The stability characteristics of VSCs under reactive power control needs to be investigated for a weak system connection. Moreover, some specially designed control strategies for HB-MMCs or HY-MMCs, such as the CCSC or the DC fault-ride-through control, may also affect the small-signal stability and cause some difference. The comparative study needs to be conducted to obtain an in-depth understanding.

The contributions of this paper are as follows:

1) In this paper, the stability analysis with special consideration on both rectifier and inverter operation is carried out for VSCs under constant reactive power and DC voltage control, which is a more general control strategy for high-power MMC-HVDC projects.

2) The stability comparison of TL-VSC, HB-MMC, and HY-MMC is conducted for the first time under weak AC system integration, emphasizing the instability caused by excessive rectified or inverted active power.

3) Both single-terminal-based frequency-domain impedance analysis and point-to-point-based time-domain modal analysis have been employed, and the results are compared. Detailed dynamics of the control system including PLL, sampling filters and various current controllers are modeled in the impedance and state-space small-signal models.

4) Methods of retuning control parameters, including PLL, ACC, and DCC, are summarized to improve stability for different operation states.

The paper is organized as follows. A brief derivation of the dynamic models for the three VSCs is displayed in Section II. The single-terminal-based impedance analysis is presented in Section III. Section IV demonstrates the root locus and PF analysis with increasing the active power penetration based on

a typical point-to-point system. The stability analysis results are validated by electromagnetic simulations in Section V. The improvement of stability by parameter adjustment is analyzed and validated in Section VI. The conclusion is finally drawn in Section VII.

II. Dynamic Models

The topologies for TL-VSC, HB-MMC, and HY-MMC are depicted in Fig. 1. The AC-side circuits of the three VSCs are the same. The parameters are listed in the Appendix.

A. Electrical system model

1) *The AC-side equivalent circuits*

Based on the equivalent circuit shown in Fig. 1 (a), the dynamics of the AC current i can be obtained by applying KVL:

$$u_s / K_T = R_{tot} i + L_{tot}\, \mathrm{d}i/\mathrm{d}t + u_v \tag{1}$$

where $R_{tot}=(R_s+R_T)/K_T^2$. For HB/HY-MMC, $L_{tot}=(L_s+L_T)/K_T^2$; for TL-VSC, $L_{tot}=L_{ac}+(L_s+L_T)/K_T^2$.

For TL-VSCs, u_v can be linked to u_{dc} by the modulation signal m[8]:

$$u_v = m u_{dc}/2 \tag{2}$$

Define the rotating frame xy which is synchronized with the PCC voltage u_p, and u_v can be expressed in xy frame as:

$$u_{vx} = M_x u_{dc}/2 \tag{3}$$

$$u_{vy} = M_y u_{dc}/2 \tag{4}$$

While for HB-MMC or HY-MMC, u_v is associated with the upper or lower arm output voltage [20]:

$$u_v = u_{dc}/2 + R_{arm} i_{up} + L_{arm}\, \mathrm{d}i_{up}/\mathrm{d}t - m_p u_{cp}^{\Sigma} \tag{5}$$

$$u_v = -u_{dc}/2 + R_{arm} i_{dn} + L_{arm}\, \mathrm{d}i_{dn}/\mathrm{d}t + m_n u_{cn}^{\Sigma} \tag{6}$$

By adding up (5) and (6), we can obtain:

$$u_v = \frac{R_{arm}}{2} i + \frac{L_{arm}}{2}\frac{\mathrm{d}i}{\mathrm{d}t} + \underbrace{\left(m_n u_{cn}^{\Sigma} - m_p u_{cp}^{\Sigma}\right)/2}_{e_v} \tag{7}$$

The last item in (7) is defined as the internal AC output voltage of MMC e_v. Similarly, e_v can be expressed in xy frame:

$$e_{vx} = \left(\frac{m_n u_{cn}^{\Sigma} - m_p u_{cp}^{\Sigma}}{2}\right)_x, e_{vy} = \left(\frac{m_n u_{cn}^{\Sigma} - m_p u_{cp}^{\Sigma}}{2}\right)_y \tag{8}$$

By exploring the x and y components of the items in (8), we can obtain [18]:

$$\begin{bmatrix} e_{vx} \\ e_{vy} \end{bmatrix} = \begin{bmatrix} \frac{M_x}{4} & \frac{M_y}{4} & \frac{M_{x2}-2M_{dc}}{4} & \frac{M_{y2}}{4} & \frac{M_x}{2} \\ \frac{-M_y}{4} & \frac{M_x}{4} & \frac{M_{y2}}{4} & -\frac{M_{x2}+2M_{dc}}{4} & \frac{M_y}{2} \end{bmatrix} \mathbf{u}_{\mathbf{c}}^{\Sigma} \tag{9}$$

where $\mathbf{u}_{\mathbf{c}}^{\Sigma} = \left[u_{cx2}^{\Sigma}, u_{cy2}^{\Sigma}, u_{cx}^{\Sigma}, u_{cy}^{\Sigma}, u_{c0}^{\Sigma}\right]^T$. M_{dc} is usually set to be constant 1 in HB-MMCs. On the contrary, M_{dc} can be flexibly regulated in HY-MMCs due to the negative insertion of the sub-modules [18].

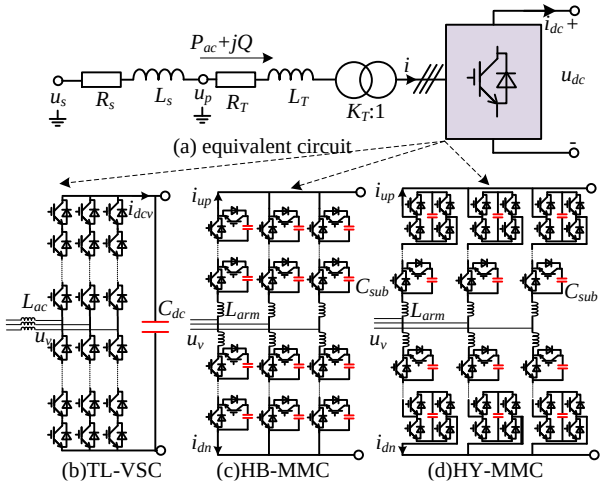

Fig. 1. Equivalent circuit and topologies of the three VSCs.

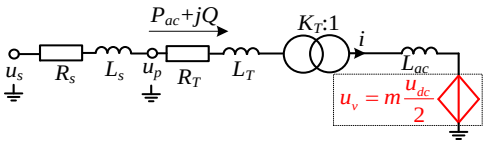

(a) AC-side equivalent circuit for TL-VSCs

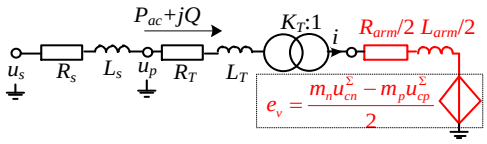

(b) AC-side equivalent circuit for HB-MMCs or HY-MMCs

Fig. 2. AC-side equivalent circuits.

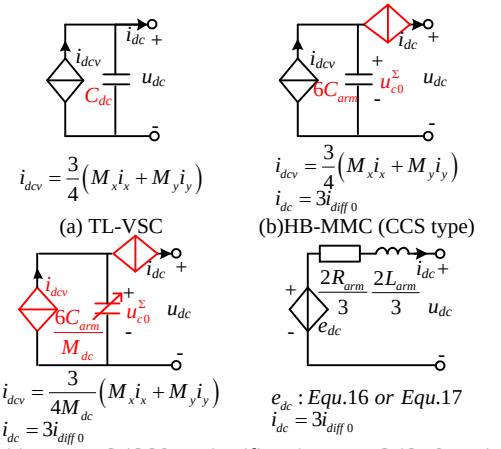

Fig. 3. DC-side equivalent circuits.

Based on the above derivation, the AC-side equivalent circuits for TL-VSC, HB-MMC, and HY-MMC are depicted in Fig. 2. The expressions of the AC-side controlled voltages are similar, which are the productions of the modulation signal and the capacitor voltage.

2) *The DC-side equivalent circuit*

For TL-VSC, the dynamics of capacitor voltage u_{dc} can be

described as:

$$C_{dc}\frac{\mathrm{d}u_{dc}}{\mathrm{d}t}=i_{dc}-i_{dcv} \tag{10}$$

The DC current i_{dcv} is generally obtained by considering the active power balance between the AC and DC side:

$$1.5\left(u_{vx}i_x+u_{vy}i_y\right)=u_{dc}i_{dcv} \tag{11}$$

Substitute (3) and (4) into (11), and we can obtain:

$$i_{dcv}=0.75\left(M_x i_x+M_y i_y\right) \tag{12}$$

Based on the above derivation, the DC-side equivalent circuit for TL-VSC is depicted in Fig. 3 (a). The CCS is generated by the production of the modulation signals and the AC current, and i_{dc} is provided from the DC network.

For HB-MMC or HY-MMC, the dynamics of the capacitor voltage can be described as [20]:

$$C_{arm}\frac{\mathrm{d}u_{cp}^{\Sigma}}{\mathrm{d}t}=-m_p i_{up} \tag{13}$$

where C_{arm}=C_{sub}/N_{sub}.

If we expand the expressions of the variables in (13) under the rotating *xy* frame, and retain only the DC components, we can get the dynamics of the DC total capacitor voltage. For HB-MMC, we have[19]:

$$6C_{arm}\frac{\mathrm{d}u_{c0}^{\Sigma}}{\mathrm{d}t}=\underbrace{0.75\left(M_x i_x+M_y i_y\right)}_{i_{dcv}}-\underbrace{3i_{diff\,0}}_{i_{dc}} \tag{14}$$

The first term on the right side of equation (14) is represented by i_{dcv}, and the second item is denoted as i_{dc}. Then the DC-side equivalent circuit based on CCS for HB-MMC is depicted in Fig. 3 (b). Different from TL-VSC, i_{dc} in HB-MMC is decided by its state variable i_{diff0} instead of the DC network. The DC voltage of the equivalent capacitance $6C_{arm}$ is equal to u_{c0}^{Σ}, instead of the DC terminal voltage.

While for HY-MMC, due to the variable M_{dc}, the dynamic expression for u_{c0}^{Σ} is different from that of HB-MMC:

$$\frac{6C_{arm}}{M_{dc}}\frac{\mathrm{d}u_{c0}^{\Sigma}}{\mathrm{d}t}=\underbrace{\frac{3}{4M_{dc}}\left(M_x i_x+M_y i_y\right)}_{i_{dcv}}-\underbrace{3i_{diff\,0}}_{i_{dc}} \tag{15}$$

As shown in Fig. 3 (c), the expressions for the equivalent capacitance and the CCS i_{dcv} in HY-MMC are different from those in HB-MMC, both of which are related to M_{dc}.

The voltages across the CCS in Fig. 3 (b) and (c) remain to be solved, which makes it difficult to analyze. Instead, we can obtain the dynamic equation for i_{dc} by subtracting (5) and (6), and retaining only the DC component. For HB-MMC, we have[19][20]:

$$\begin{aligned}&\frac{2L_{arm}}{3}\frac{\mathrm{d}i_{dc}}{\mathrm{d}t}=\frac{2R_{arm}}{3}i_{dc}+u_{dc}+\\&\underbrace{u_{c0}^{\Sigma}-\frac{1}{2}\left(M_x u_{cx}^{\Sigma}+M_y u_{cy}^{\Sigma}+M_{x2}u_{cx2}^{\Sigma}+M_{y2}u_{cy2}^{\Sigma}\right)}_{e_{dc}}\end{aligned} \tag{16}$$

For HY-MMC, we have[18]:

$$\begin{aligned}&\frac{2L_{arm}}{3}\frac{\mathrm{d}i_{dc}}{\mathrm{d}t}=\frac{2R_{arm}}{3}i_{dc}+u_{dc}+\\&\underbrace{M_{dc}u_{c0}^{\Sigma}-\frac{1}{2}\left(M_x u_{cx}^{\Sigma}+M_y u_{cy}^{\Sigma}+M_{x2}u_{cx2}^{\Sigma}+M_{y2}u_{cy2}^{\Sigma}\right)}_{e_{dc}}\end{aligned} \tag{17}$$

The equivalent CVS e_{dc} for HB-MMC and HY-MMC is respectively given in (16) and (17), which is defined as the internal DC output voltage. According to (16) and (17), we can obtain the CVS-based equivalent circuit for HB-MMC or HY-MMC, as shown in Fig. 3 (d).

B. Control system model

The classical vector-based current control for the three topologies are depicted in Fig. 4. The TL-VSC only adopts ACC, and the control target α for the *d* axis outer loop can be selected as either P_{ac} or u_{dc}. In comparison, HB-MMC additionally adopts CCSC. The DC current for TL-VSC or HB-MMC is constrained by implicit AC/DC active power balance with the relatively constant DC voltage.

For HY-MMC, an extra DCC can be employed to actively control the DC fault current[7]. The outer loop control target α for the *d* axis is fixed as the average capacitor voltage $u_{c,avg}$, which is equal to u_{c0}^{Σ}, and the outer loop control target β for the DC-axis can be selected as P_{ac} or u_{dc}. A similar internal energy control for HB-MMC can be found in [21], which is proved to be effective in suppressing the oscillation between the DC bus capacitor and the sub-module capacitor.

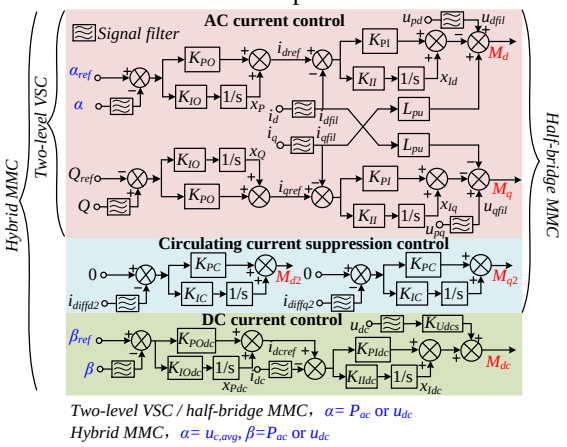

Fig. 4. Current controller structure for three types of VSCs.

TABLE I

COMPARISON OF THE SMALL-SIGNAL MODELS FOR VSCS

State variables (order)		TL-VSC	HB-MMC	HY-MMC
AC current		i_x, i_y	i_x, i_y	i_x, i_y
VSC electric system	Capacitor voltage	u_{dc}	$\mathbf{u}_c^{\Sigma}$	$\mathbf{u}_c^{\Sigma}$
	Circulating current	-	i_{diffx2}, i_{diffy2}	i_{diffx2}, i_{diffy2}
	DC current	-	i_{diff0}	i_{diff0}
VSC control system	ACC	x_P,x_{Id},x_Q,x_{Iq}	x_P,x_{Id},x_Q,x_{Iq}	x_P,x_{Id},x_Q,x_{Iq}
	CCSC	-	(2)	(2)
	DCC	-	-	x_{Pdc}, x_{Idc}
	PLL	(2)	(2)	(2)
	Signal filters	(14)	(18)	(22)
Total order for single converter		21	34	40

The control system is modeled under the *dq* rotating frame, which is aligned with the measured PCC voltage of the PLL. The relation between the *xy* frame and the *dq* frame can be derived based on the PLL dynamics. The dynamic model for the control system can be directly obtained based on block diagrams of the controller, which is not presented in detail in this paper. The dynamic models for PLL and signal filters can be addressed in [19]. By combining the dynamic models of different sub-systems, the whole small-signal model can be obtained in a modular way. The total orders for the closed-loop models of single TL-VSC, HB-MMC and HY-MMC are respectively 21, 34 and 40 in this paper, as shown in TABLE I.

III. Impedance Analysis

In this section, the *dq* impedance models for TL-VSC, HB-MMC and HY-MMC are derived and compared based on the small-signal model. The converters operate under the constant DC voltage and reactive power control mode. The output reactive power is set to be 10% of the rated capacity. The SCR of the connected AC system is set to be 2, which can be classified as the weak AC system. The parameters for the VSCs and AC system can be found in the Appendix. The parameters of the PLL, ACC and signal filters are kept the same for three VSCs, which can be also found in the Appendix. The time-delays of the sampled electric signals are simplified and represented by the second-order low-pass filters, as derived in the Appendix.

Limited by space, the derivations of the AC impedance models are provided in the Appendix, and the detailed derivation process can be referred to [11]-[13]. The impact of the DC-side network is neglected [10] [12] [28] by setting the small-signal expressions for the DC current or DC active power to be zeros. The *dq* impedances of VSCs and the AC system are denoted as:

$$\mathbf{Z_{con}} = \begin{bmatrix} Z_{condd} & Z_{condq} \\ Z_{conqd} & Z_{conqq} \end{bmatrix} \tag{18}$$

$$\mathbf{Z_g} = \begin{bmatrix} Z_{gdd} & Z_{gdq} \\ Z_{gqd} & Z_{gqq} \end{bmatrix} = \begin{bmatrix} R_s + sL_s & -\omega_0 L_s \\ \omega_0 L_s & R_s + sL_s \end{bmatrix} \tag{19}$$

A. Impedance analysis based on bode plots

The AC active power is gradually increased, and $\boldsymbol{Z_{con}}$ is calculated iteratively. By checking the phase differences of the *dq* components of $\boldsymbol{Z_{con}}$ and $\boldsymbol{Z_g}$ where they have points of intersection in the magnitude response, the stability can be judged [15]. If the magnitude of $\boldsymbol{Z_g}$ is going to be larger than $\boldsymbol{Z_{con}}$ and the phase difference is larger than 180 °, the system is unstable.

For the inverter status, the values of P_{ac} for TL-VSC, HB-MMC and HY-MMC are all set to be 60% of the rated capacity. The frequency responses of *dq* AC impedances within 0.1Hz~1kHz are depicted in Fig. 5 (a). The negative resistance zones are shadowed. It can be seen that the frequency responses of Z_{conqq} for the VSCs are almost identical, and the frequency responses of Z_{condd} are similar. The Z_{condd} is close to a pure positive resistance within low-frequency range (<5Hz). It becomes a negative resistance within medium-frequency range (<100Hz), and finally approaches a pure inductance as the frequency increases above 1kHz. While Z_{conqq} contains a negative resistance within about 200Hz, and becomes a positive resistance afterward.

Though there exist points of intersection between the magnitude curves of Z_{gdd} and Z_{condd}, the corresponding phase differences are all within 180 °. Instead, the instability is identified according to Z_{qq}, as depicted in Fig. 6 (a). For TL-VSC, Z_{gqq} becomes larger than Z_{conqq} from 188.3Hz. The phases of Z_{gqq} and Z_{conqq} at 188.3Hz are separately 88.84 ° and -95.87 °, making up a phase difference of 184.7 °, which indicates the system is unstable. For HB-MMC, Z_{gqq} becomes larger than Z_{conqq} from 187.7Hz, with a corresponding phase difference of 184.2 °. For HY-MMC, Z_{gqq} becomes larger than Z_{conqq} from 187.6Hz, with a corresponding phase difference of 183.8 °.

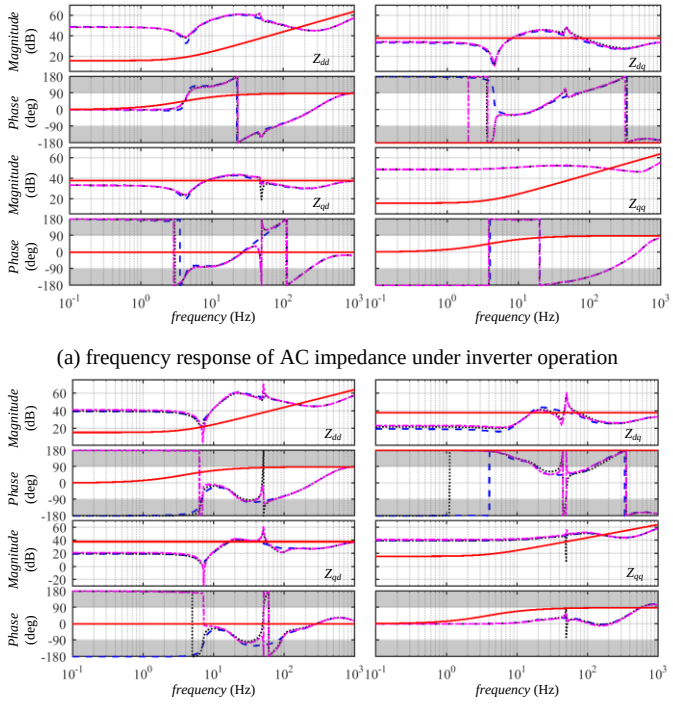

(a) frequency response of AC impedance under inverter operation

(b) frequency response of AC impedance under rectifier operation

TL-VSC HB-MMC HY-MMC AC Grid *negative resistance zone*

Fig. 5. Comparison of AC impedances.

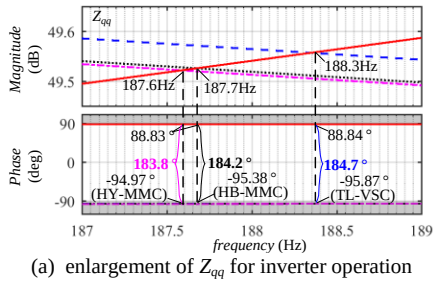

(a) enlargement of Z_{qq} for inverter operation

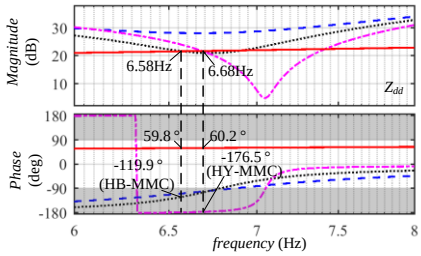

(b) enlargement of Z_{dd} for rectifier operation

TL-VSC HB-MMC HY-MMC AC Grid *negative resistance zone*

Fig. 6. Stability assessment.

For the rectifier status, P_{ac} of TL-VSC, HB-MMC and HY-MMC are all set to be 100% of the rated capacity. The frequency responses of *dq* AC impedance are depicted in Fig. 5 (b). Z_{condd} is close to a pure negative resistance within low-frequency range (<7Hz). It becomes a positive resistance afterward, and finally approaches a pure inductance as the frequency increases above 1kHz. Z_{conqq} contains a positive resistance within 500Hz.

There also exist points of intersection between the magnitudes of Z_{gqq} and Z_{conqq}, but the corresponding phase differences are all within 180°. Instead, the instability is identified according to Z_{dd}, as shown in Fig. 6 (b). TL-VSC is stable since Z_{gdd} keeps smaller than Z_{condd}. For HB-MMC, the magnitude curves of Z_{condd} and Z_{gdd} cross at 6.58Hz, and Z_{gdd} becomes bigger than Z_{condd} afterward. But the phase difference at 6.58Hz is within 180°, indicating a stable system. For HY-MMC, the magnitude curves cross at 6.68Hz, and the corresponding phase difference is above 180°, indicating an unstable system.

B. Impedance analysis based on generalized Nyquist criterion

The stability can also be predicted by applying the generalized Nyquist criterion (GNC) to the impedance ratio $\mathbf{Z_g/Z_{con}}$. The eigenvalue loci of $\mathbf{Z_g/Z_{con}}$ for three VSCs are depicted in Fig. 7. The values of P_{ac} under each operation state are set to be the same as those in Fig. 5. The critical point (-1,0) is marked as '+'. The two different eigenvalue loci are indicated by different arrows.

According to Fig. 7 (a), (c) and (e), the eigenvalue loci of the impedance ratio for three VSCs all encircle the point (-1, 0) clockwise, indicating instability under the inverter status.

In Fig. 7 (b) and (d), the eigenvalue loci of TL-VSC and HB-MMC do not encircle (-1, 0), indicating stable systems. While in Fig. 7 (e), the eigenvalue loci of HY-MMC encircle (-1, 0) clockwise, indicating instability.

The GNC analysis results are consistent with the bode-plot-based impedance analysis regarding stability judgment. In comparison, the bode-plot-based analysis demonstrates more intuitive results, given that the oscillation frequencies and phase margins can be obtained from the magnitude-frequency and phase-frequency response curves straightforwardly.

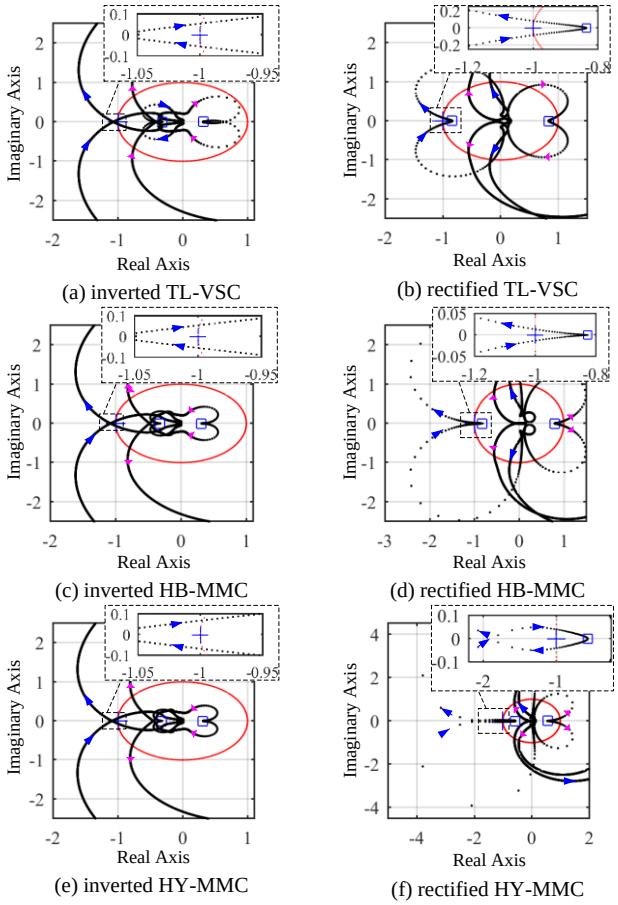

(a) inverted TL-VSC (b) rectified TL-VSC

(c) inverted HB-MMC (d) rectified HB-MMC

(e) inverted HY-MMC (f) rectified HY-MMC

Fig. 7. Nyquist diagrams of eigenvalue loci of $\mathbf{Z_g/Z_{con}}$.

IV. Modal Analysis

A two-terminal test system is employed in this section, as shown in Fig. 8. The master converter regulating the DC voltage and its reactive power is connected to the weak AC system, named as VSC1. The other terminal (VSC2) is the slave converter that controls its PCC active power and reactive power. The connected AC system 2 is with SCR of 20. The capacitance and inductance of TL-VSCs and HB/HY-MMCs satisfy:

$$C_{dc} = 6C_{arm} \tag{20}$$

$$\left(L_T + L_{ac}K_T^2\right)_{TL-VSC} = \left(L_T + 0.5L_{arm}K_T^2\right)_{HB/HY-MMC} \tag{21}$$

A. Root locus analysis

Let the master converter respectively operate as an inverter or rectifier, and gradually increase the active power. The root loci for three topologies are depicted in Fig. 9 (a)-(c). As shown in the left column, with the rise of the inverted power into the weak AC system, all three test systems become unstable. Despite the different numbers and distribution of the eigenvalues, the oscillation frequencies of the unstable modes under the critical active power are respectively close to each other. The eigenvalue analysis complies with frequency-

domain analysis in the previous section.

As shown in the right column of Fig. 9, with the rise of the rectified power from the weak AC system, all three test systems become unstable. The critical values of the active power and the corresponding oscillation frequencies of the unstable modes are noted in the figures, which are different from each other. However, the oscillation frequencies have the same order of magnitudes, which are all several Hz.

B. Participation factor analysis of state variables

PF analysis is usually conducted to distinguish the most involved state variables regarding certain unstable modes. The PF of *k*th state variable towards *i*th eigenvalue is calculated [22]:

$$p_{ki} = v_{ki}u_{ki} \Big/ \boldsymbol{v}_i^T \boldsymbol{u}_i \tag{22}$$

where $\boldsymbol{v}_i$ and $\boldsymbol{u}_i$ are respectively the left and right eigenvectors for the *i*th eigenvalue, and v_{ki} and u_{ki} are respectively the elements on the *k*th row and *i*th column of $\boldsymbol{v}_i$ and $\boldsymbol{u}_i$.

The values of the inverted and rectified active power are all set to be 60%, and corresponding PF analysis results for the unstable modes are respectively displayed in Fig. 10 (a)-(c). The total orders of the test two-terminal systems are respectively 49, 75 and 87, including the models for AC currents and DC networks. The corresponding state variables for different sub-systems are labeled along the horizon axis in Fig. 10. Based on the distribution of the PF, similarity and difference can be obtained.

First of all, the mainly participated state variables under the inverter and rectifier status are different from each other, which holds for all the three topologies. Specifically, the unstable mode under the inverter status is primarily concerned with the reactive component of the AC current or measured PCC voltage, which are noted as i_y and u_{qfil}. In contrast, the unstable mode under the rectifier status is mainly related to the state variable of the outer loop for *d*-axis x_P and the DC component of the capacitor voltage (u_{dc} or u_{c0}^{Σ}). Notice that x_P in the master VSCs is closely linked to the integration of u_{dc} or u_{c0}^{Σ}, so it can be inferred that the instability is closely concerned with u_{dc} or u_{c0}^{Σ}.

Secondly, the unstable mode under the inverter status can be classified as a local oscillation mode for all three VSCs: the related state variables only belong to the converter connected to the weak AC system. In comparison, the unstable mode under the rectifier status is an interactive oscillation mode for TL-VSC and HB-MMC: the unstable mode is related to the u_{dc} or u_{c0}^{Σ} of the other terminal connected to the strong AC system. This conclusion is consistent with [23], which reveals that the coupling effect between the AC and DC side dynamics cannot be ignored for studying low-frequency resonance of VSC. However, for HY-MMC, the unstable mode under the rectifier status is still a local oscillation mode, indicating less affected by the coupling effect.

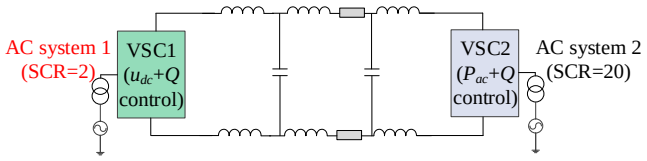

Fig. 8. Topology of the tested two-terminal system.

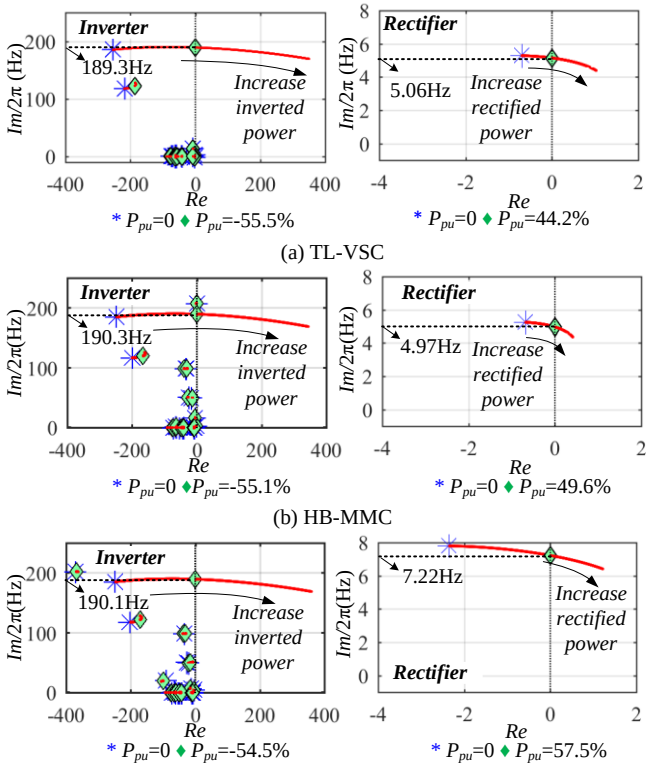

Fig. 9. Root locus analysis with increasing the active power.

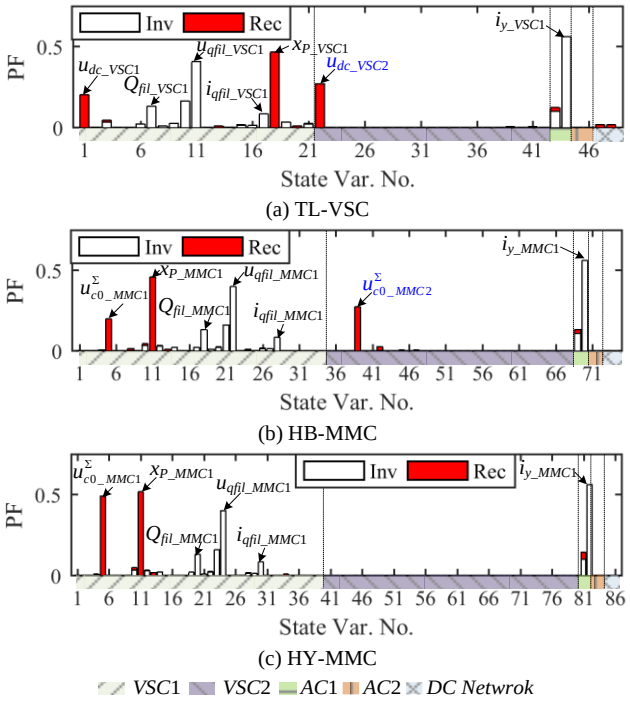

Fig. 10. Participation factor analysis under rectifier and inverter status.

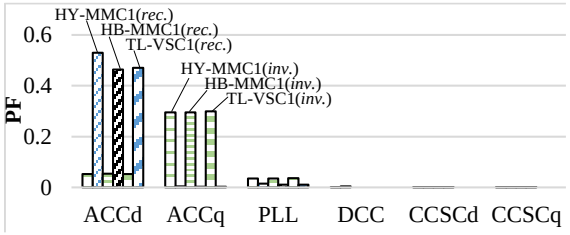

Fig. 11. Participation factor of different control loops versus the critical unstable modes under rectifier and inverter status.

C. PF analysis of different control loops

In order to figure out the participation of the control loops, such as the ACC *d*-axis (ACCd), ACC *q*-axis (ACCq), PLL, CCSC or DCC, we aggregate the PFs of state variables related to the corresponding control loop, including the inputs and the integration units. Taking the example of ACCd, the control output is M_d. According to Fig. 4, the small-signal model of M_d can be expressed as:

$$\Delta M_d = \Delta u_{dfil} + L_{pu}\Delta i_{qfil} - \Delta x_{Id} + K_{PI}\left(\Delta i_{dfil} - \Delta x_P + K_{PO}\Delta u_{dcfil}\right) \quad (23)$$

Then, the PF of ACCd can be equivalently calculated as:

$$p_{ACCd} = p_{u_{dfil}} + L_{pu}\,p_{i_{qfil}} - p_{x_{Id}} + K_{PI}\left(p_{i_{dfil}} - p_{x_P} + K_{PO}\,p_{u_{dcfil}}\right) \quad (24)$$

where p_x indicates the PF of x.

The calculation results are displayed in Fig. 11. The equivalent PF is not evident for PLL, DCC or CCSC, which means the controllability and observability of their outputs to the instability are little. Instead, to design the additional damping control for oscillation depression, the damping control input/output is better selected from/ injected into the ACCd under rectifier status or ACCq under inverter status.

TABLE II
SUMMARY OF MODAL ANALYSIS RESULTS

Status	Item	TL-VSC	HB-MMC	HY-MMC
inverter	critical P_{ac}	55.5%	55.1%	54.5%
	osc. freq.	189.3Hz	190.3Hz	190.1Hz
	state variables	i_{y_VSC1}, u_{qfil_VSC1}	i_{y_MMC1}, u_{qfil_MMC1}	i_{y_MMC1}, u_{qfil_MMC1}
	mode	Local	Local	Local
rectifier	critical P_{ac}	44.2%	49.6%	57.5%
	osc. freq.	5.06Hz	4.97Hz	7.22Hz
	state variables	x_{P_VSC1}, u_{dc_VSC1}, u_{dc_VSC2}	x_{P_MMC1}, $u^{\Sigma}_{c0\_MMC1}$, $u^{\Sigma}_{c0\_MMC2}$	x_{P_MMC1}, $u^{\Sigma}_{c0\_MMC1}$
	mode	Interactive	Interactive	Local

D. Comparison with the AC impedance analysis

The frequency-domain impedance analysis in Section III shows that all the VSCs in inverter operation may suffer from an oscillation of hundreds-of-Hz at 60% active power transmission, which complies with the root locus analysis. In contrast, for the rectifier operation state, only HY-MMC may have an oscillation of several Hz at 100% active power transmission. The rectified TL-VSC and HB-MMC remain stable even at 100% active power transmission, which is not consistent with the modal analysis. The potential reason for this deviation on stability judgment is that the AC impedance model neglects the impact of the DC network and other terminals. The coupling of AC and DC networks is suggested to be considered for analyzing such low-frequency oscillation under rectifier operation [23]. Since the DC-side variables are closely related to the instability under rectifier operation, the neglect of the DC dynamics may cause an inaccurate estimation of the instability.

While for HY-MMC, the converter internal energy, as well as the DC current, is explicitly and independently regulated in different control loops, leading to more decoupled dynamics between AC and DC sides. Hence, the AC impedance analysis for HY-MMC is able to effectively predict the instability under both inverter and rectifier operation states.

E. Summary

The numbers of eigenvalues for the three types of VSCs are different from each other. Despite that MMCs produce more eigenvalues, the critical eigenvalues that induce instability are similar. The summary of the modal analysis is displayed in TABLE II. It can be concluded that,

- The instability triggered by increasing the inverted active power for the three types of VSCs shows the same characteristics.
- The instability triggered by increasing the rectified active power for the TL-VSC and HB-MMC shows the same characteristics. The difference for HY-MMC is that the unstable mode is only related to the local converter.

V. SIMULATION VERIFICATION OF INSTABILITY

In this section, the electromagnetic models of the test system under three VSC topologies are established in PSCAD/EMTDC. The instability is simulated, and corresponding oscillation is analyzed. The waveforms of the PCC active power (P_{acpu}), the DC current (i_{dcpu}), the reactive power (Q_{pu}), the DC voltage (u_{dcpu}), phase A current (i_{a_VSC1}, i_{a_VSC2}, i_{a_MMC1}, i_{a_MMC2}) and the average capacitor voltage(u^{Σ}_{c0}) are depicted. Harmonic percent (*Harm*.%) of the oscillation waveforms is analyzed.

A. TL-VSC

As shown in Fig. 12 (a), the inverted active power P_{acpu} of the TL-VSC1 gradually increases to 58%, and the oscillation is triggered, which is reflected in Q_{pu}, u_{dcpu} and i_{dcpu}. Fourier analysis shows that the dominant oscillation frequency is 192.4Hz, which is close to the modal calculation result of 189.0Hz at P_{acpu}= -58%. Meanwhile, according to the frequency coupling of the rotating *dq* frame and static *ABC* frame, 143Hz and 193Hz harmonics appear in the AC current of VSC1, and the AC current of VSC2 contains little harmonics, as shown in Fig. 12 (c).

The rectified active power of VSC1 gradually increases to 45%, and the oscillations in u_{dcpu}, i_{dcpu} and P_{acpu} finally diverge, while Q_{pu} remains stable, as shown in Fig. 12 (b). Fourier analysis shows that the dominant oscillation frequency is 5.00Hz, which is consistent with the modal calculation result of 5.05Hz at P_{acpu}=45%. Meanwhile, 45Hz and 55Hz harmonics are observed in the AC current of VSC1, and the AC current of

VSC2 contains little harmonics.

It can be seen that under both scenarios, the oscillation appears in the DC voltage and DC current of the master TL-VSC1, which means the oscillation can be propagated into the DC network and affects the other terminals. However, the oscillation cannot pass the other converters and influence the corresponding connected AC system.

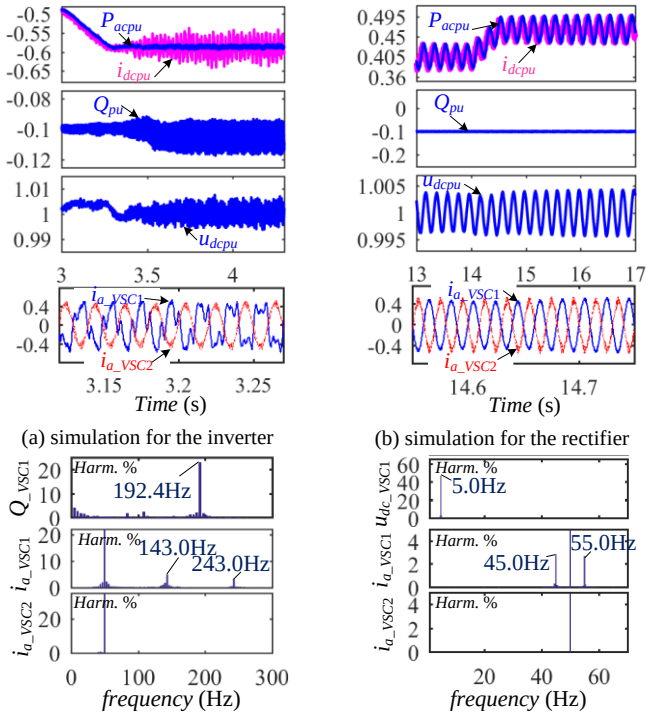

(a) simulation for the inverter (b) simulation for the rectifier

(c) harmonic analysis for the inverter (d) harmonic analysis for the rectifier

Fig. 12. Simulation results of TL-VSC1 under weak AC grid integration.

B. HB-MMC

As shown in Fig. 13 (a), the inverted active power of HB-MMC1 gradually increases to 55%. It is evident that diverging oscillation with high-frequency appears in Q_{pu}, u_{dcpu} and i_{dcpu}, while mild oscillation is observed in both $u^{\Sigma}_{c0\_MMC1}$ and $u^{\Sigma}_{c0\_MMC2}$. The dominant frequency of the oscillation is 208.7Hz, which is close to the modal calculation result of 190.3Hz. Meanwhile, corresponding harmonics can be observed in the AC current of HB-MMC1, but no harmonics appear in the AC current of HB-MMC2, as shown in Fig. 13 (c).

The rectified active power rises to 50%, as shown in Fig. 13 (b), and low-frequency oscillation occurs in u_{dcpu}, i_{dcpu}, and $u^{\Sigma}_{c0\_MMC1}$, with the reactive power staying relatively stable. The dominant frequency of the oscillation is 4.91Hz, which is consistent with the modal calculation result of 4.97Hz. Corresponding harmonics appear in the AC current of HB-MMC1 by frequency coupling. Moreover, $u^{\Sigma}_{c0\_MMC2}$ contains low-frequency oscillation, which accords with the PF analysis in Fig. 10 (b), but no harmonics emerge in the AC current of HB-MMC2.

It can be similarly concluded that the oscillation of HB-MMC1 is propagated through the DC network and affects the other terminals. However, the oscillation is effectively absorbed and blocked by the sub-module capacitors of other MMCs, leaving the connected AC system unaffected.

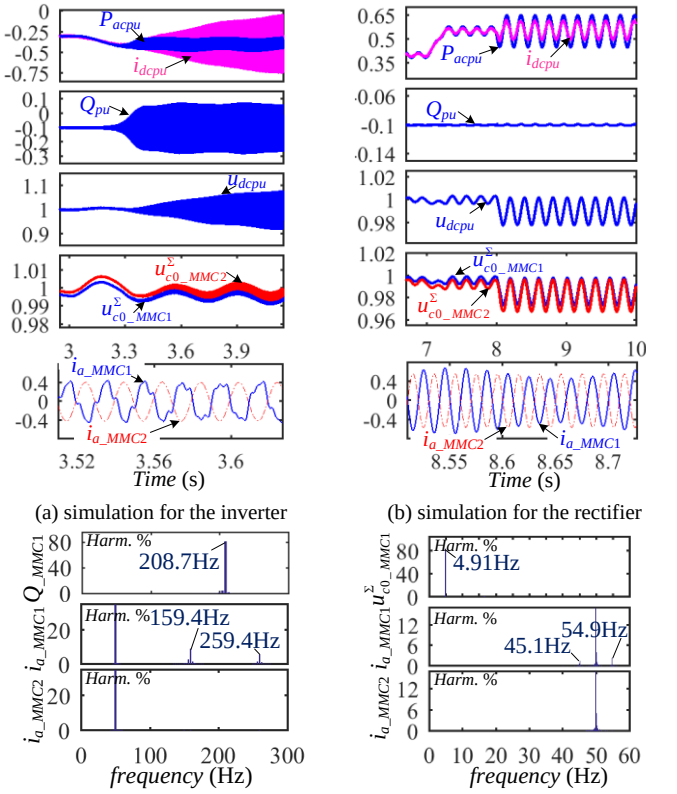

(a) simulation for the inverter (b) simulation for the rectifier

(c) harmonic analysis for the inverter (d) harmonic analysis for the rectifier

Fig. 13. Simulation results of HB-MMC1 under weak AC grid integration.

C. HY-MMC

The instability under the inverter and rectifier status for the HY-MMC1 is simulated, as shown in Fig. 14 (a) and (b) respectively. Compared to the simulation results for the HB-MMC1 in Fig. 13 (a) and (b), apparently, the DC current and DC voltage in Fig. 14 are nearly kept unaffected. As shown in Fig. 14 (b), the average capacitor voltage of MMC1 is oscillating, while that of MMC2 stays stable. Separate Fourier analysis to the oscillating reactive power and the average capacitor voltage reveals the dominant frequency components are respectively 186.3Hz and 7.21Hz, which are consistent with the modal calculation results of 190.1Hz and 7.22Hz. Meanwhile, corresponding harmonics appear in the AC current of HY-MMC1 due to frequency coupling, and the AC current of HY-MMC2 stays undistorted, as shown in Fig. 14 (c) and (d).

Compared to TL-VSC1 or HB-MMC1, for HY-MMC1, the oscillation cannot be propagated through the DC network. The oscillation or harmonics only appear on the AC-side, and are entirely absorbed and blocked by the master HY-MMC1, leaving the rest of the DC system unaffected.

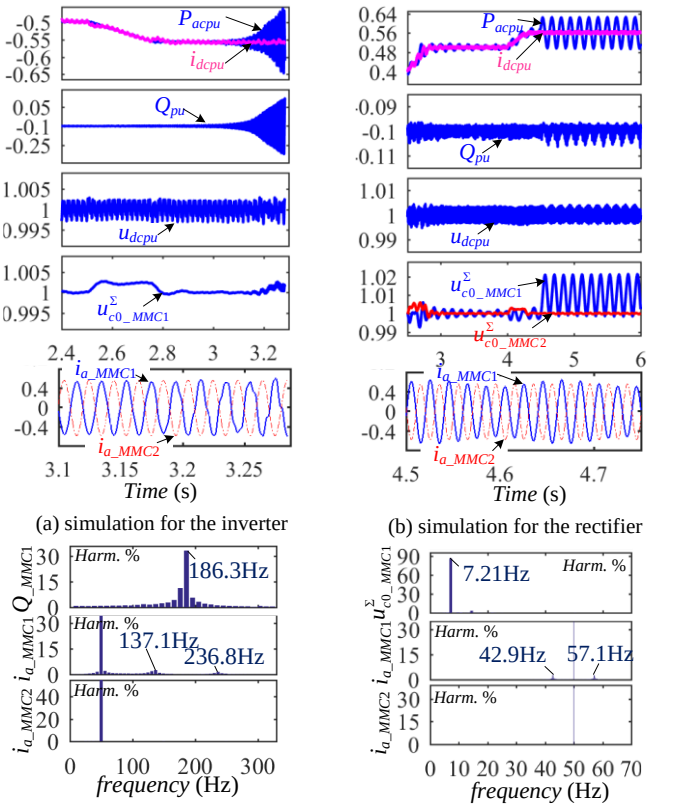

(a) simulation for the inverter

(b) simulation for the rectifier

(c) harmonic analysis for the inverter

(d) harmonic analysis for the rectifier

Fig. 14. Simulation results of HY-MMC1 under weak AC grid integration.

VI. Improvement of Stability

A. Impact of the reactive power

In practice, the unity power factor is normally required for the VSC-HVDC operation in order to make full use of the converter capacity. For weak AC grid integration, VSCs may be required to output reactive power to support the AC voltage [24][25]. The relationship between u_s, u_p, P_{ac} and Q can be obtained as [25]:

$$u_p^4+\left(2P_{ac}R_s-2Q\omega L_s-u_s^2\right)u_p^2+\left(P_{ac}^2+Q^2\right)\left(\omega^2L_s^2+R_s^2\right)=0 \quad (25)$$

To guarantee real solutions of u_p to (25), P_{ac} and Q of the operation point should satisfy:

$$\Delta=\left(2P_{ac}R_s-2Q\omega L_s-u_s^2\right)^2-4\left(P_{ac}^2+Q^2\right)\left(\omega^2L_s^2+R_s^2\right)\geq 0 \quad (26)$$

The feasible operating points are calculated and gathered in Fig. 15, where the negative sign indicates capacitive reactive power from VSCs. The maximum apparent power is set to be 120% of the rated capacity. The magnitude of corresponding u_p at each operation point is indicated by the color bar.

For a fixed reactive power value, the mathematically maximum active power can be obtained to ensure feasible operation points. The default reactive power for the VSCs in this paper is set to be -10%, then the calculated maximum active power is 118% for the inverter operation and 101% for the rectifier operation according to Fig. 15.

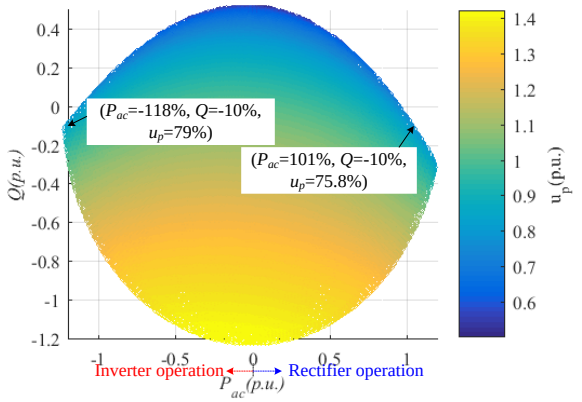

Fig. 15 Feasible operation zone considering the PCC voltage.

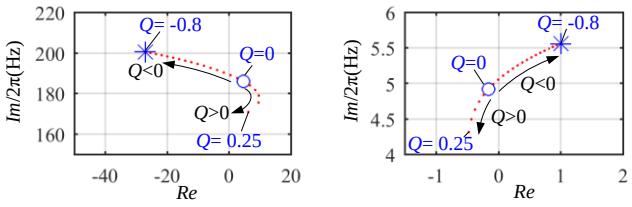

(a) inverter operation

(b) rectifier operation

Fig. 16. Root locus analysis of varying the reactive power for TL-VSC.

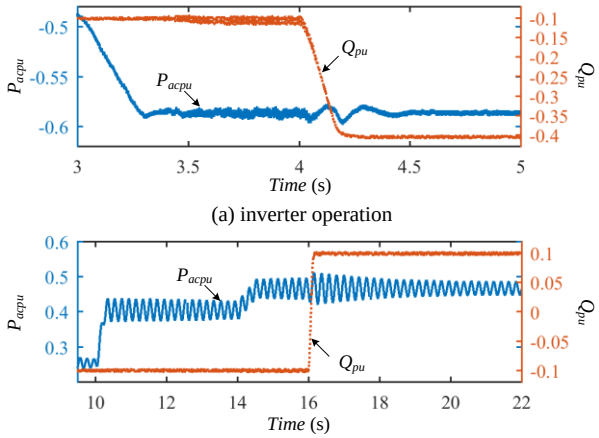

(a) inverter operation

(b) rectifier operation

Fig. 17. Electromagnetic simulation of varying the reactive power.

Besides the above steady-state analysis, the impact of the reactive power on the small-signal stability is studied through the system root locus analysis. The calculation results only for TL-VSC is demonstrated. The results are similar for HB-MMC and HY-MMC. The values for the active power are selected as the critical values in Fig. 9 (a), i.e., 55.5% for the inverter operation and 44.2% for the rectifier operation.

According to Fig. 15, at such active power transmission, the feasible reactive power can be varied from -80% to 25%. Then the variation range of the reactive power for the root locus analysis is determined. As shown in Fig. 16 (a), under inverter operation, VSCs should output more reactive power to improve stability. In contrast, under rectifier operation, VSCs should reduce reactive power output, or even absorb more reactive power, as shown in Fig. 16 (b). The requirements of the reactive power for stability improvement are opposite under different operation states.

The corresponding electromagnetic simulation results are depicted in Fig. 17. As shown in Fig. 17 (a), the high-frequency oscillation in the active and reactive power is effectively suppressed when the output reactive power is increased from 10% to 40%. As shown in Fig. 17 (b), the amplitude of the low-frequency oscillation in the active power is gradually decreasing as the reactive power is varied from -10% to 10%.

Compared with the simulation results in Fig. 19, adjusting the reactive power is not as quick and efficient as adjusting the control parameters in suppressing the oscillation. Moreover, with more output reactive power, the PCC voltage may be greatly increased, which may introduce the over-modulation problem for HB-MMC and HY-MMC, due to insufficient sub-modules to build the required AC voltage.

B. Sensitivity study of control parameters

Retuning of the control parameters can be useful for stability improvement. In [26]-[28], the speeding up of the AC voltage controller and the slowing down of PLL are suggested for the VSCs under DC voltage and AC voltage control mode. While in this paper, the VSCs are under a different control mode. Different results on retuning the control parameters are obtained, as demonstrated below.

The operating point are set as the critical states in Fig. 9 (a)-(d). By separately varying the control parameters, the system root loci can be obtained, and the movement of the original unstable mode can be observed. The calculation results are depicted in Fig. 18.

As shown in Fig. 18 (a), for the TL-VSC inverter, by decreasing the default value of the proportional gain for PLL K_{Ppll}, the unstable mode moves to the left-half-plane, which indicates the improvement of stability. Similarly, decreasing the proportional and integration gain of ACC inner loop (K_{PI}, K_{II}) or outer loop (K_{PO}, K_{IO}) can also help improve stability under inverter operation. The results for TL-VSC rectifier, as well as HB-MMC and HY-MMC, can be found in Fig. 18 (b)-(g).

The comparative results are demonstrated in TABLE III. It can be seen that:

(1) The operation state lays a great influence on PLL tuning. The control of PLL should be slowed down under inverter operation and accelerated under rectifier operation.

(2) Similarly to PLL tuning, the outer loop of ACC should be slowed down in *q*-axis under inverter operation and sped up in *d*-axis under rectifier operation.

Generally, under inverter status, the control gains for PLL and ACC, including K_{Ppll}, K_{PI}, K_{II}, K_{PO} and K_{IO}, need to be reduced to restore stability. In contrast, K_{Ppll} and K_{PO} need to be increased under rectifier status. Besides, the adjustment of DCC parameter for HY-MMC is only useful under rectifier status.

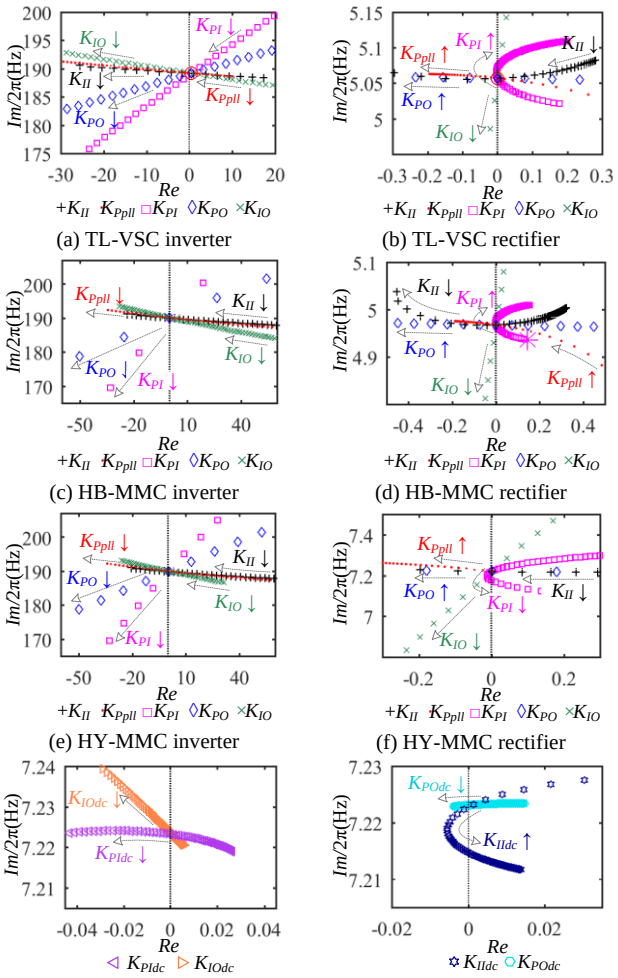

Fig. 18. Root locus of different control parameters.

TABLE III
SUGGESTED ADJUST DIRECTION OF CONTROL PARAMETERS FROM DEFAULTS

Parameters \ VSC		TL-VSC		HB-MMC		HY-MMC	
		Inv.	*Rec.*	*Inv.*	*Rec.*	*Inv.*	*Rec.*
PLL	K_{Ppll}	↓	↑	↓	↑	↓	↑
ACC	K_{PI}	↓	↑	↓	↑	↓	↓
	K_{II}	↓	↓	↓	↓	↓	↓
	K_{PO}	↓	↑	↓	↑	↓	↑
	K_{IO}	↓	↓	↓	↓	↓	↓
DCC	K_{PIdc}	-	-	-	-	-	↓
	K_{IIdc}	-	-	-	-	-	↑
	K_{POdc}	-	-	-	-	-	↓
	K_{IOdc}	-	-	-	-	-	↓

'↓' indicates decreasing, '↑' indicates increasing

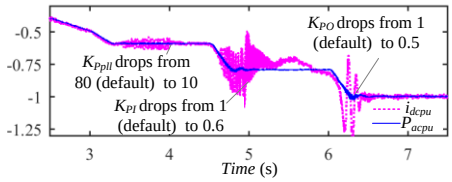

(a) inverter TL-VSC

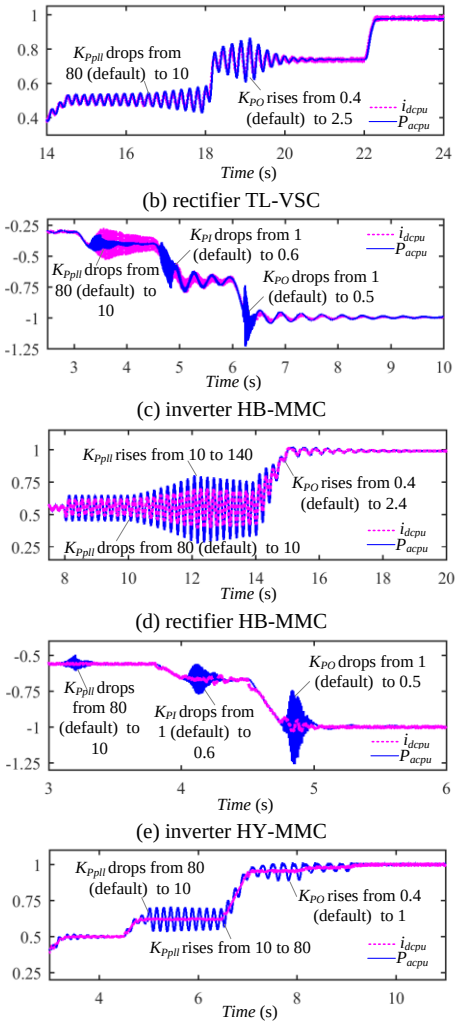

Fig. 19. Simulation results for validating effectiveness of parameter adjust.

C. Simulation validation

The effectiveness of adjusting control parameters is validated by simulation in PSCAD/EMTDC platform. The results are shown in Fig. 19.

As shown in Fig. 19 (a), (c) and (e), when high-frequency oscillation occurs in the inverted AC active power or DC current, K_{Ppll} is reduced from default 80 to 10, and the oscillation is effectively depressed. With the active power continuing rising, high-frequency oscillation emerges again, and K_{PI} or K_{PO} are successively reduced. The oscillation can be suppressed. The inverted active power finally achieves full capacity, as guaranteed by the calculation in Section VI. A.

As shown in Fig. 19 (b), (d) and (f), when low-frequency oscillation occurs in the rectified AC active power or DC current, if we still reduce K_{Ppll} as we do under the inverter status, the oscillation is deteriorated with its amplitude increasing. After K_{PO} is increased, the oscillation can be suppressed, and the rectified power successfully achieves full capacity, which is also confirmed by the calculation in Section VI. A.

VII. Conclusion

This paper investigates the small-signal stability of TL-VSC, HB-MMC and HY-MMC under weak AC system integration by impedance analysis, root locus analysis, participation factor analysis and electromagnetic simulation.

Even though the small-signal model for the HB/HY-MMC is more complicated with considering the internal dynamics of the capacitor voltage and circulating current, PF analysis shows that except the DC capacitor voltage, other internal state variables of MMCs, such as the harmonics of the circulating current and total sub-module capacitor voltage, are hardly related to the instability.

The single-terminal impedance analysis for the three types of VSCs complies with the eigenvalue analysis results under the inverter operation state. However, it is unable to identify the instability under the rectifier operation state for TL-VSC and HB-MMC, which is due to the neglect of interaction with other DC terminals. While the unstable modes of HY-MMC are only related to local variables. It is due to the direct DC current control, which makes them decoupled from DC networks.

The two-terminal stability analysis results reveal that the stability characteristics of three types of VSCs under the inverter operation status are similar, including the frequencies of the oscillation, the mainly participating state variables and the effective parameter adjustment method. While under the rectifier operation status, the difference lies in the penetrability of the instability to other terminals. For TL-VSC and HB-MMC, the unstable modes are interactive, involving DC capacitor voltages from other converters. As for HY-MMC, the unstable mode is local, indicating the instability cannot affect other terminals through DC networks.

Appendix

A. Relations of time-delays and second-order low-pass filters

The time-delay τ can be expressed as:

$$D_{delay}(s) = e^{-\tau s} \tag{A1}$$

Applying *Taylor* series expansion to (A1) yields:

$$D_{delay}(s) = \frac{1}{1+\tau s+\frac{\tau^2 s^2}{2!}+\frac{\tau^3 s^3}{3!}+\cdots} \tag{A2}$$

When τ is really small, we can neglect the higher orders, for example, the third order and above, then (A2) is simplified as:

$$D_{delay}(s) \approx \frac{1}{1+\tau s+\frac{\tau^2 s^2}{2!}} \tag{A3}$$

(A3) is exactly the transfer function of a second-order low-pass filter with the damping ratio of 0.707 and the cutting-off frequency $f_c = \sqrt{2}/2\pi\tau$.

B. AC impedance of the TL-VSC

The small-signal model of *i*:

$$\left[\begin{matrix}\Delta u_{px}\\ \Delta u_{py}\end{matrix}\right]_{\Delta \mathbf{u_{pxy}}}=\frac{K_T u_{dc0}}{2}\left[\begin{matrix}\Delta M_x\\ \Delta M_y\end{matrix}\right]_{\Delta \mathbf{M_{xy}}}+\frac{K_T}{2}\left[\begin{matrix}M_{x0}\\ M_{y0}\end{matrix}\right]\Delta u_{dc}+\frac{1}{K_T}\left[\begin{matrix}R_T+sL_{tot} & -\omega_0 L_{tot}\\ \omega_0 L_{tot} & R_T+sL_{tot}\end{matrix}\right]_{\mathbf{G_i}}\left[\begin{matrix}\Delta i_x\\ \Delta i_y\end{matrix}\right] \tag{A4}$$

where $L_{tot}=L_T+K_T^2 L_{ac}$.

According to (A4), $\Delta\mathbf{i_{xy}}=[\Delta i_x, \Delta i_y]^{\mathrm{T}}$ can be expressed as:

$$\Delta\mathbf{i_{xy}}=\left[-\mathbf{G_i}^{-1}\frac{K_T u_{dc0}}{2}\right]_{\mathbf{G_{iMxy}}}\Delta\mathbf{M_{xy}}+\left[-\mathbf{G_i}^{-1}\right]_{\mathbf{G_{iuxy}}}\Delta\mathbf{u_{pxy}}+\left[-\mathbf{G_i}^{-1}\frac{K_T}{2}\left[\begin{matrix}M_{x0}\\ M_{y0}\end{matrix}\right]\right]_{\mathbf{G_{iudc}}}\Delta u_{dc} \tag{A5}$$

Neglecting the dynamics of the DC current from the DC network, the small-signal mode of u_{dc} is,

$$C_{dc}s\Delta u_{dc}=\frac{3}{2K_T}\Delta\left(\frac{u_{px}i_x+u_{py}i_y}{u_{dc}}\right) \tag{A6}$$

According to (A6), Δu_{dc} can be further expressed as:

$$\Delta u_{dc}=\left[\frac{3\left[u_{px0}\ u_{py0}\right]}{2\left(u_{dc0}C_{dc}s+i_{dc0}\right)}\right]_{\mathbf{G_{udci}}}\Delta\mathbf{i_{xy}}+\left[\frac{3\left[i_{x0}\ i_{y0}\right]}{2\left(u_{dc0}C_{dc}s+i_{dc0}\right)}\right]_{\mathbf{G_{udcu}}}\Delta\mathbf{u_{pxy}} \tag{A7}$$

The small-signal for the ACC output $[\Delta M_d, \Delta M_q]^{\mathrm{T}}$:

$$\left[\begin{matrix}\Delta M_d\\ \Delta M_q\end{matrix}\right]=\left[\begin{matrix}\Delta u_{dfil}\\ \Delta u_{qfil}\end{matrix}\right]+\left[\begin{matrix}G_{in} & L_{pu}\\ -L_{pu} & G_{in}\end{matrix}\right]\left[\begin{matrix}\Delta i_{dfil}\\ \Delta i_{qfil}\end{matrix}\right]-\left[\begin{matrix}0\\ G_{in}G_{out}\end{matrix}\right]\Delta Q_{fil}+\left[\begin{matrix}G_{in}G_{out}\\ 0\end{matrix}\right]\Delta u_{dcfil} \tag{A8}$$

where $G_{in}=K_{PI}+K_{II}/s$, $G_{out}=K_{PO}+K_{IO}/s$.

Consider the transfer functions of the signal filters, such as the AC voltage,

$$\left[\begin{matrix}\Delta u_{dfil}\\ \Delta u_{qfil}\end{matrix}\right]_{\Delta\mathbf{u_{dqfil}}}=\left[\frac{1/U_{base}}{1+\tau_u s+\tau_u^2 s^2/2!}\right]_{D_u}\left[\begin{matrix}\Delta u_{pd}\\ \Delta u_{pq}\end{matrix}\right]_{\Delta\mathbf{u_{pdq}}} \tag{A9}$$

where $\tau_u=\sqrt{2}/2\pi f_{uac}$, f_{uac} is the cutting-off frequency for the AC voltage sampling filter. U_{base} is the base value for the AC voltage. Similarly, we can obtain:

$$\left[\begin{matrix}\Delta i_{dfil}\\ \Delta i_{qfil}\end{matrix}\right]_{\Delta\mathbf{i_{dqfil}}}=\left[\frac{1/I_{base}}{1+\tau_i s+\tau_i^2 s^2/2!}\right]_{D_i}\left[\begin{matrix}\Delta i_d\\ \Delta i_q\end{matrix}\right]_{\Delta\mathbf{i_{dq}}} \tag{A10}$$

$$\Delta Q_{fil}=\left[\frac{1/S_{base}}{1+\tau_Q s+\tau_Q^2 s^2/2!}\right]_{D_Q}\Delta Q \tag{A11}$$

$$\Delta u_{dcfil}=\left[\frac{1/U_{dcbase}}{1+\tau_{udc}s+\tau_{udc}^2 s^2/2!}\right]_{D_{udc}}\Delta u_{dc} \tag{A12}$$

Then $\Delta\mathbf{M_{dq}}=[\Delta M_d, \Delta M_q]^{\mathrm{T}}$ can be further expressed as:

$$\Delta\mathbf{M_{dq}}=\left[\left[\begin{matrix}1,0\\ 0,1\end{matrix}\right]D_u\right]_{\mathbf{G_{Mdqudq}}}\Delta\mathbf{u_{pdq}}+\left[\left[\begin{matrix}0\\ -G_{in}G_{out}\end{matrix}\right]D_Q\right]_{\mathbf{G_{MdqQ}}}\Delta Q+\left[\left[\begin{matrix}G_{in} & L_{pu}\\ -L_{pu} & G_{in}\end{matrix}\right]D_i\right]_{\mathbf{G_{Mdqidq}}}\Delta\mathbf{i_{dq}}+\left[\left[\begin{matrix}G_{in}G_{out}\\ 0\end{matrix}\right]D_{udc}\right]_{\mathbf{G_{Mdqudc}}}\Delta u_{dc} \tag{A13}$$

The small-signal model for Q:

$$\Delta Q=\left(3\left[-i_{y0}, i_{x0}\right]/2K_T\right)_{\mathbf{G_{Qu}}}\Delta\mathbf{u_{pxy}}+\left(3\left[u_{py0}, -u_{px0}\right]/2K_T\right)_{\mathbf{G_{Qi}}}\Delta\mathbf{i_{xy}} \tag{A14}$$

The small-signal model for PLL:

$$\Delta\theta=\left(\left[-\frac{1}{s}\left(K_{Ppll}+K_{Ipll}/s\right)\right]D_u\left[0,1\right]\right)_{\mathbf{G_{PLLu}}}\Delta\mathbf{u_{pdq}} \tag{A15}$$

$[\Delta i_d, \Delta i_q]^{\mathrm{T}}$ can be expressed as:

$$\left[\begin{matrix}\Delta i_d\\ \Delta i_q\end{matrix}\right]=\left[\begin{matrix}\cos\theta_0 & \sin\theta_0\\ -\sin\theta_0 & \cos\theta_0\end{matrix}\right]_{\mathbf{C_{\theta 1}}}\left[\begin{matrix}\Delta i_x\\ \Delta i_y\end{matrix}\right]+\left[\begin{matrix}-\sin\theta_0 & \cos\theta_0\\ -\cos\theta_0 & -\sin\theta_0\end{matrix}\right]_{\mathbf{C_{\theta 2}}}\left[\begin{matrix}i_{x0}\\ i_{y0}\end{matrix}\right]_{\mathbf{i_{xy0}}}\Delta\theta \tag{A16}$$

Substitute (A15) into (A16), and $[\Delta i_d, \Delta i_q]^{\mathrm{T}}$ can be obtained:

$$\Delta\mathbf{i_{dq}}=\mathbf{C_{\theta 1}}\Delta\mathbf{i_{xy}}+\left(\mathbf{C_{\theta 2}}\mathbf{i_{xy0}}\mathbf{G_{PLLu}}\right)_{\mathbf{G_{idqudq}}}\Delta\mathbf{u_{pdq}} \tag{A17}$$

Similarly, $[\Delta u_{pd}, \Delta u_{pq}]^{\mathrm{T}}$ can be obtained as:

$$\Delta\mathbf{u_{pdq}}=\left[\left(\mathbf{I}-\mathbf{C_{\theta 2}}\mathbf{u_{pxy0}}\mathbf{G_{PLLu}}\right)^{-1}\mathbf{C_{\theta 1}}\right]_{\mathbf{G_{udquxy}}}\Delta\mathbf{u_{pxy}} \tag{A18}$$

$[\Delta M_x, \Delta M_y]^{\mathrm{T}}$ can be expressed as:

$$\left[\begin{matrix}\Delta M_x\\ \Delta M_y\end{matrix}\right]_{\Delta\mathbf{M_{xy}}}=\left[\begin{matrix}\cos\theta_0 & -\sin\theta_0\\ \sin\theta_0 & \cos\theta_0\end{matrix}\right]_{\mathbf{C_{03}}}\left[\begin{matrix}\Delta M_d\\ \Delta M_q\end{matrix}\right]+\left[\begin{matrix}-\sin\theta_0 & -\cos\theta_0\\ \cos\theta_0 & -\sin\theta_0\end{matrix}\right]_{\mathbf{C_{04}}}\left[\begin{matrix}M_{d0}\\ M_{q0}\end{matrix}\right]_{\mathbf{M_{dq0}}}\Delta\theta \tag{A19}$$

Substituting (A14), (A17) and (A18) into (A13) yields:

$$\Delta\mathbf{M_{dq}}=\left[\left(\mathbf{G_{Mdqudq}}+\mathbf{G_{Mdqidq}}\mathbf{G_{idqudq}}\right)\mathbf{G_{udquxy}}+\mathbf{G_{MdqQ}}\mathbf{G_{Qu}}\right]_{\mathbf{G_{Mdquxy}}}\Delta\mathbf{u_{pxy}}+\mathbf{G_{Mdqudc}}\Delta u_{dc}+\left(\mathbf{G_{MdqQ}}\mathbf{G_{Qi}}+\mathbf{G_{Mdqidq}}\mathbf{C_{\theta 1}}\right)_{\mathbf{G_{Mdqixy}}}\Delta\mathbf{i_{xy}} \tag{A20}$$

Substituting (A7) and (A20) into (A19) yields:

$$\Delta\mathbf{M_{xy}}=\left[\mathbf{C_{03}}\left(\mathbf{G_{Mdqixy}}+\mathbf{G_{Mdqudc}}\mathbf{G_{udci}}\right)\right]_{\mathbf{G_{Mxyi}}}\Delta\mathbf{i_{xy}}+\left[\mathbf{C_{\theta 3}}\left(\mathbf{G_{Mdquxy}}+\mathbf{G_{Mdqudc}}\mathbf{G_{udcu}}\right)+\mathbf{C_{\theta 4}}\mathbf{M_{dq0}}\mathbf{G_{PLLu}}\mathbf{G_{udquxy}}\right]_{\mathbf{G_{Mxyu}}}\Delta\mathbf{u_{pxy}} \tag{A21}$$

Substitute (A7) and (A21) into (A5), and we can obtain the dq impedance as:

$$\mathbf{Z_{con}}=K_T\left(\mathbf{G_{iMxy}}\mathbf{G_{Mxyu}}+\mathbf{G_{iudc}}\mathbf{G_{udcu}}+\mathbf{G_{iuxy}}\right)^{-1}\cdot\left(\mathbf{I}-\mathbf{G_{iMxy}}\mathbf{G_{Mxyi}}-\mathbf{G_{iudc}}\mathbf{G_{udci}}\right) \tag{A22}$$

C. AC impedance of the HB-MMC

The small-signal model of i:

$$\left[\begin{matrix}R_{tot}+sL_{tot} & -\omega_0 L_{tot}\\ \omega_0 L_{tot} & R_{tot}+sL_{tot}\end{matrix}\right]_{\mathbf{G_i}}\left[\begin{matrix}\Delta i_x\\ \Delta i_y\end{matrix}\right]+\left[\begin{matrix}\Delta e_{vx}\\ \Delta e_{vy}\end{matrix}\right]=\frac{1}{K_T}\left[\begin{matrix}\Delta u_{px}\\ \Delta u_{py}\end{matrix}\right] \tag{A23}$$

where $L_{tot}=L_{arm}/2+L_T/K_T^2$, $R_{tot}=R_{arm}/2+R_T/K_T^2$.

Based on (9) in the context, $\Delta\mathbf{e}_{\mathbf{vxy}}=[\Delta e_{vx},\Delta e_{vy}]^{\mathrm{T}}$ are obtained:

$$\Delta\mathbf{e}_{\mathbf{vxy}}=\begin{bmatrix}\frac{u_{cx0}^{\Sigma}}{4} & \frac{u_{cy0}^{\Sigma}}{4}\\ \frac{-u_{cy0}^{\Sigma}}{4} & \frac{u_{cx0}^{\Sigma}}{4}\end{bmatrix}_{\mathbf{G_{evM2}}}\begin{bmatrix}\Delta M_{x2}\\ \Delta M_{y2}\end{bmatrix}_{\Delta\mathbf{M_{xy2}}}+\begin{bmatrix}\frac{2u_{c00}^{\Sigma}+u_{px20}^{\Sigma}}{4} & \frac{u_{cy20}^{\Sigma}}{4}\\ \frac{u_{cy20}^{\Sigma}}{4} & \frac{2u_{c00}^{\Sigma}-u_{cx20}^{\Sigma}}{4}\end{bmatrix}_{\mathbf{G_{evM}}}\begin{bmatrix}\Delta M_x\\ \Delta M_y\end{bmatrix}_{\Delta\mathbf{M_{xy}}}+\begin{bmatrix}\frac{M_{x0}}{4} & \frac{M_{y0}}{4} & \frac{M_{x20}-2}{4} & \frac{M_{y20}}{4} & \frac{M_{x0}}{2}\\ \frac{-M_{y0}}{4} & \frac{M_{x0}}{4} & \frac{M_{y20}}{4} & -\frac{M_{x20}+2}{4} & \frac{M_{y0}}{2}\end{bmatrix}_{\mathbf{G_{evuc}}}\Delta\mathbf{u}_{\mathbf{c}}^{\Sigma} \tag{A24}$$

The small-signal model of $\Delta\mathbf{u}_{\mathbf{c}}^{\Sigma}$ is [19]:

$$\mathbf{G_{uc}}\Delta\mathbf{u}_{\mathbf{c}}^{\Sigma}=\mathbf{G_{uci0}}\Delta i_{diff\,0}+\mathbf{G_{ucidiff}}\Delta\mathbf{i}_{\mathbf{diffxy2}}+\mathbf{G_{ucM}}\Delta\mathbf{M}_{\mathbf{xy}}+\mathbf{G_{ucM2}}\Delta\mathbf{M}_{\mathbf{xy2}}+\mathbf{G_{uci}}\Delta\mathbf{i}_{\mathbf{xy}} \tag{A25}$$

where,

$$\mathbf{G_{uc}}=\begin{bmatrix}C_{arm}s & -2\omega C_{arm} & 0 & 0 & 0\\ 2\omega C_{arm} & C_{arm}s & 0 & 0 & 0\\ 0 & 0 & C_{arm}s & -\omega C_{arm} & 0\\ 0 & 0 & \omega C_{arm} & C_{arm}s & 0\\ 0 & 0 & 0 & 0 & C_{arm}s\end{bmatrix}$$

$$\mathbf{G_{uci0}}=\frac{1}{2}\begin{bmatrix}M_{x20} & M_{y20} & M_{x0} & M_{y0} & -1\end{bmatrix}^{\mathrm{T}}$$

$$\mathbf{G_{ucidiff}}=\frac{1}{4}\begin{bmatrix}-2 & 0 & M_{x0} & -M_{y0} & M_{x20}\\ 0 & -2 & M_{y0} & M_{x0} & M_{y20}\end{bmatrix}^{\mathrm{T}}$$

$$\mathbf{G_{ucM}}=\frac{1}{8}\begin{bmatrix}i_{x0} & i_{y0} & 4i_{diff\,00} & 0 & i_{x0}\\ -i_{y0} & i_{x0} & 0 & 4i_{diff\,00} & i_{y0}\end{bmatrix}^{\mathrm{T}}$$

$$\mathbf{G_{ucM2}}=\frac{1}{8}\begin{bmatrix}4i_{diff\,00} & 0 & i_{x0} & -i_{y0} & 0\\ 0 & 4i_{diff\,00} & i_{y0} & i_{x0} & 0\end{bmatrix}^{\mathrm{T}}$$

$$\mathbf{G_{uci}}=\frac{1}{8}\begin{bmatrix}M_{x0} & M_{y0} & M_{x20}-2 & M_{y20} & M_{x0}\\ -M_{y0} & M_{x0} & M_{y20} & -M_{x20}-2 & M_{y0}\end{bmatrix}^{\mathrm{T}}$$

The small-signal model of $\Delta\mathbf{i}_{\mathbf{diffxy2}}=[\Delta i_{diffx2},\Delta i_{diffy2}]^{\mathrm{T}}$ is [19]:

$$\begin{bmatrix}R_{arm}+L_{arm}s & -2\omega L_{arm}\\ 2\omega L_{arm} & R_{arm}+L_{arm}s\end{bmatrix}_{\mathbf{G_{idiff}}}\Delta\mathbf{i}_{\mathbf{diffxy2}}=\begin{bmatrix}\frac{1}{2} & 0 & -\frac{M_{x0}}{4} & \frac{M_{y0}}{4} & -\frac{M_{x20}}{2}\\ 0 & \frac{1}{2} & -\frac{M_{y0}}{4} & -\frac{M_{x0}}{4} & -\frac{M_{y20}}{2}\end{bmatrix}_{\mathbf{G_{idiffuc}}}\Delta\mathbf{u}_{\mathbf{c}}^{\Sigma}+\begin{bmatrix}-\frac{u_{cx0}^{\Sigma}}{4} & \frac{u_{cy0}^{\Sigma}}{4}\\ -\frac{u_{cy0}^{\Sigma}}{4} & -\frac{u_{cx0}^{\Sigma}}{4}\end{bmatrix}_{\mathbf{G_{idiffM}}}\Delta\mathbf{M}_{\mathbf{xy}}+\begin{bmatrix}-\frac{u_{c00}^{\Sigma}}{2} & 0\\ 0 & -\frac{u_{c00}^{\Sigma}}{2}\end{bmatrix}_{\mathbf{G_{idiffM2}}}\Delta\mathbf{M}_{\mathbf{xy2}} \tag{A26}$$

The small-signal model of Δi_{diff0} [19]:

$$\left(sL_{arm}+R_{arm}\right)_{G_{i0}}\Delta i_{diff\,0}=\left(-\frac{1}{2}\right)_{G_{i0udc}}\Delta u_{dc}+\begin{bmatrix}\frac{-M_{x20}}{4} & \frac{-M_{y20}}{4} & \frac{-M_{x0}}{4} & \frac{-M_{y0}}{4} & \frac{1}{2}\end{bmatrix}_{\mathbf{G_{i0uc}}}\Delta\mathbf{u}_{\mathbf{c}}^{\Sigma}+\begin{bmatrix}\frac{-u_{cx0}^{\Sigma}}{4} & \frac{-u_{cy0}^{\Sigma}}{4}\end{bmatrix}_{\mathbf{G_{i0M}}}\Delta\mathbf{M}_{\mathbf{xy}}+\begin{bmatrix}\frac{-u_{cx20}^{\Sigma}}{4} & \frac{-u_{cy20}^{\Sigma}}{4}\end{bmatrix}_{\mathbf{G_{i0M2}}}\Delta\mathbf{M}_{\mathbf{xy2}} \tag{A27}$$

The small-signal models of PLL, $\Delta\mathbf{i}_{\mathbf{dq}}$ and $\Delta\mathbf{u}_{\mathbf{pdq}}$ are the same as the TL-VSC. The small-signal model for ACC is the same as (A20), then $\Delta\mathbf{M}_{\mathbf{xy}}$ can be expressed as:

$$\Delta\mathbf{M}_{\mathbf{xy}}=\left(\mathbf{C_{\theta 3}G_{Mdqixy}}\right)_{\mathbf{G_{Mxyi}}}\Delta\mathbf{i}_{\mathbf{xy}}+\left(\mathbf{C_{\theta 3}G_{Mdqudc}}\right)_{\mathbf{G_{Mxyudc}}}\Delta u_{dc}+\left(\mathbf{C_{\theta 3}G_{Mdquxy}}+\mathbf{C_{\theta 4}M_{dq0}G_{PLLu}G_{udquxy}}\right)_{\mathbf{G_{Mxyu}}}\Delta\mathbf{u}_{\mathbf{pxy}} \tag{A28}$$

The small-signal model of CCSC:

$$\begin{bmatrix}\Delta M_{d2}\\ \Delta M_{q2}\end{bmatrix}_{\Delta\mathbf{M_{dq2}}}=\left(\begin{bmatrix}G_{CC} & 0\\ 0 & G_{CC}\end{bmatrix}D_{idiff}\right)_{\mathbf{G_{Mdq2}}}\begin{bmatrix}\Delta i_{diffd2}\\ \Delta i_{diffq2}\end{bmatrix}_{\Delta\mathbf{i_{diffdq2}}} \tag{A29}$$

where $G_{CC}=K_{PC}+K_{IC}/s$. D_{idiff} is the transfer function of the signal filter for the circulating current.

$\Delta\mathbf{i_{diffdq2}}$ can be expressed as:

$$\Delta\mathbf{i}_{\mathbf{diffdq2}}=\begin{bmatrix}\cos 2\theta_0 & \sin 2\theta_0\\ -\sin 2\theta_0 & \cos 2\theta_0\end{bmatrix}_{\mathbf{C_{05}}}\Delta\mathbf{i}_{\mathbf{diffxy2}} \tag{A30}$$

$[\Delta M_{x2},\Delta M_{y2}]^{\mathrm{T}}$ can be expressed as:

$$\begin{bmatrix}\Delta M_{x2}\\ \Delta M_{y2}\end{bmatrix}_{\Delta\mathbf{M_{xy2}}}=\begin{bmatrix}\cos 2\theta_0 & -\sin 2\theta_0\\ \sin 2\theta_0 & \cos 2\theta_0\end{bmatrix}_{\mathbf{C_{07}}}\begin{bmatrix}\Delta M_{d2}\\ \Delta M_{q2}\end{bmatrix}+\begin{bmatrix}-2\sin 2\theta_0 & -2\cos 2\theta_0\\ 2\cos 2\theta_0 & -2\sin 2\theta_0\end{bmatrix}_{\mathbf{C_{08}}}\begin{bmatrix}M_{d20}\\ M_{q20}\end{bmatrix}_{\mathbf{M_{dq20}}}\Delta\theta \tag{A31}$$

Substitute (A29) and (A30) into (A31), and we can get:

$$\Delta\mathbf{M}_{\mathbf{xy2}}=\left(\mathbf{C_{\theta 7}G_{Mdq2}C_{05}}\right)_{\mathbf{G_{Mxy2i2}}}\Delta\mathbf{i}_{\mathbf{diffxy2}}+\left(\mathbf{C_{\theta 8}M_{dq20}G_{PLLu}G_{udquxy}}\right)_{\mathbf{G_{Mxy2u}}}\Delta\mathbf{u}_{\mathbf{pxy}} \tag{A32}$$

By neglecting the deviation of DC active power, we get:

$$0=3u_{dc0}\Delta i_{diff\,0}+i_{dc0}\Delta u_{dc} \tag{A33}$$

Then we get a group of algebra equations in complex field:

$$\begin{bmatrix}\mathbf{G_i} & \mathbf{G_{evuc}} & \mathbf{0}_{2*2} & \mathbf{G_{evM}} & \mathbf{G_{evM2}} & \mathbf{0}_{2*1} & \mathbf{0}_{2*1}\\ \mathbf{G_{uci}} & \mathbf{-G_{uc}} & \mathbf{G_{ucidiff}} & \mathbf{G_{ucM}} & \mathbf{G_{ucM2}} & \mathbf{G_{uci0}} & \mathbf{0}_{5*1}\\ \mathbf{0}_{2*2} & \mathbf{G_{idiffuc}} & \mathbf{-G_{idiff}} & \mathbf{G_{idiffM}} & \mathbf{G_{idiffM2}} & \mathbf{0}_{2*1} & \mathbf{0}_{2*1}\\ \mathbf{G_{Mxyi}} & \mathbf{0}_{2*5} & \mathbf{0}_{2*2} & \mathbf{-I}_{2*2} & \mathbf{0}_{2*2} & \mathbf{0}_{2*1} & \mathbf{G_{Mxyudc}}\\ \mathbf{0}_{2*2} & \mathbf{0}_{2*5} & \mathbf{G_{Mxy2i2}} & \mathbf{0}_{2*2} & \mathbf{-I}_{2*2} & \mathbf{0}_{2*1} & \mathbf{0}_{2*1}\\ \mathbf{0}_{1*2} & \mathbf{G_{i0uc}} & \mathbf{0}_{1*2} & \mathbf{G_{i0M}} & \mathbf{G_{i0M2}} & -G_{i0} & G_{i0udc}\\ \mathbf{0}_{1*2} & \mathbf{0}_{1*5} & \mathbf{0}_{1*2} & \mathbf{0}_{1*2} & \mathbf{0}_{1*2} & 3u_{dc0} & i_{dc0}\end{bmatrix}_{\mathbf{G_{ii}}}\cdot\begin{bmatrix}\Delta\mathbf{i}_{\mathbf{xy}}\\ \Delta\mathbf{u}_{\mathbf{c}}^{\Sigma}\\ \Delta\mathbf{i}_{\mathbf{diffxy2}}\\ \Delta\mathbf{M}_{\mathbf{xy}}\\ \Delta\mathbf{M}_{\mathbf{xy2}}\\ \Delta i_{diff\,0}\\ \Delta u_{dc}\end{bmatrix}=\begin{bmatrix}\mathbf{I}_{2*2}/K_T\\ \mathbf{0}_{5*2}\\ \mathbf{0}_{2*2}\\ \mathbf{-G_{Mxyu}}\\ \mathbf{-G_{Mxy2u}}\\ \mathbf{0}_{1*2}\\ \mathbf{0}_{1*2}\end{bmatrix}_{\mathbf{G_{uu}}}\Delta\mathbf{u}_{\mathbf{pxy}} \tag{A34}$$

The direct analytical expression between $\Delta\mathbf{u_{pxy}}$ and $\Delta\mathbf{i_{xy}}$ is difficult to be obtained. However, we can iteratively solve (A34) in the numerical analysis software by frequency scanning. The

first two rows of $\mathbf{G_{ii}^{-1}G_{uu}}$ are related to the AC admittance. Then we can get the AC impedance of the HB-MMC as:

$$\mathbf{Z_{con}} = K_T\left(\mathbf{G_{ii}^{-1}G_{uu}}\left([1,2],:\right)\right)^{-1} \tag{A35}$$

D.AC impedance of the HY-MMC

The AC impedance modeling for HY-MMC is similar to that of HB-MMC, except that the small-signal model of DC current controller ΔM_{dc} should be considered. The small-signal model of AC current is same as (A23). The small-signal model of $\Delta\mathbf{e_{vxy}}$ is modified as:

$$\Delta\mathbf{e_{vxy}} = \mathbf{G_{evM}}\Delta\mathbf{M_{xy}} + \mathbf{G_{evM2}}\Delta\mathbf{M_{xy2}} + \left[\frac{-u_{cx0}^{\Sigma}}{2}\ \frac{-u_{cy0}^{\Sigma}}{2}\right]^{\mathrm{T}}_{\mathbf{G_{evMdc}}}\Delta M_{dc} + \begin{bmatrix} \frac{M_{x0}}{4} & \frac{M_{y0}}{4} & \frac{M_{x20}-2M_{dc0}}{4} & \frac{M_{y20}}{4} & \frac{M_{x0}}{2} \\ \frac{-M_{y0}}{4} & \frac{M_{x0}}{4} & \frac{M_{y20}}{4} & \frac{-M_{x20}-2M_{dc0}}{4} & \frac{M_{y0}}{2} \end{bmatrix}_{\mathbf{G_{evuc}}}\Delta\mathbf{u_c^{\Sigma}} \tag{A36}$$

Similarly, ΔM_{dc} shall appear in other small-signal models.

For the total capacitor voltage:

$$\begin{aligned}\mathbf{G_{uc}}\Delta\mathbf{u_c^{\Sigma}} &= \mathbf{G_{uci0}}\Delta i_{diff\,0} + \mathbf{G_{ucidiff}}\Delta\mathbf{i_{diffxy2}} + \mathbf{G_{ucMdc}}\Delta M_{dc} \\ &\quad \mathbf{G_{ucM}}\Delta\mathbf{M_{xy}} + \mathbf{G_{ucM2}}\Delta\mathbf{M_{xy2}} + \mathbf{G_{uci}}\Delta\mathbf{i_{xy}}\end{aligned} \tag{A37}$$

$$\mathbf{G_{uci0}} = \frac{1}{2}\left[M_{x20}\ M_{y20}\ M_{x0}\ M_{y0}\ -M_{dc0}\right]^{\mathrm{T}}$$

$$\mathbf{G_{ucidiff}} = \frac{1}{4}\begin{bmatrix} -2M_{dc0} & 0 & M_{x0} & -M_{y0} & M_{x20} \\ 0 & -2M_{dc0} & M_{y0} & M_{x0} & M_{y20} \end{bmatrix}^{\mathrm{T}}$$

$$\mathbf{G_{uci}} = \frac{1}{8}\begin{bmatrix} M_{x0} & M_{y0} & M_{x20}-2M_{dc0} & M_{y20} & M_{x0} \\ -M_{y0} & M_{x0} & M_{y20} & -M_{x20}-2M_{dc0} & M_{y0} \end{bmatrix}^{\mathrm{T}}$$

$$\mathbf{G_{ucMdc}} = \left[0\,0\ \frac{-i_{x0}}{4}\ \frac{-i_{y0}}{4}\ \frac{-i_{diff\,00}}{2}\right]^{\mathrm{T}}$$

For the second harmonic of the circulating current:

$$\begin{aligned}\mathbf{G_{idiff}}\Delta\mathbf{i_{diffxy2}} &= \mathbf{G_{idiffM}}\Delta\mathbf{M_{xy}} + \mathbf{G_{idiffM2}}\Delta\mathbf{M_{xy2}} + \\ &\begin{bmatrix} \frac{M_{dc0}}{2} & 0 & -\frac{M_{x0}}{4} & \frac{M_{y0}}{4} & -\frac{M_{x20}}{2} \\ 0 & \frac{M_{dc0}}{2} & -\frac{M_{y0}}{4} & -\frac{M_{x0}}{4} & -\frac{M_{y20}}{2} \end{bmatrix}_{\mathbf{G_{idiffuc}}}\Delta\mathbf{u_c^{\Sigma}} + \\ &\left[\frac{u_{cx20}^{\Sigma}}{2}\ \frac{u_{cy20}^{\Sigma}}{2}\right]^{\mathrm{T}}_{\mathbf{G_{idiffMdc}}}\Delta M_{dc}\end{aligned} \tag{A38}$$

For the DC component of the circulating current:

$$\begin{aligned}G_{i0}\Delta i_{diff\,0} &= G_{i0udc}\Delta u_{dc} + \mathbf{G_{i0M}}\Delta\mathbf{M_{xy}} + \Delta\mathbf{G_{i0M2}}\mathbf{M_{xy2}} + \\ &\left[\frac{-M_{x20}}{4}\ \frac{-M_{y20}}{4}\ \frac{-M_{x0}}{4}\ \frac{-M_{y0}}{4}\ \frac{M_{dc0}}{2}\right]_{\mathbf{G_{i0uc}}}\Delta\mathbf{u_c^{\Sigma}} + \\ &\left(0.5u_{c00}^{\Sigma}\right)_{G_{i0Mdc}}\Delta M_{dc}\end{aligned} \tag{A39}$$

The small-signal models for PLL, signal filters and CCSC are the same as those for HB-MMC. Difference mainly exists in the modeling of ACC and DCC. The average capacitor voltage is regulated in ACC and the DC voltage is regulated in DCC, the corresponding small-signal models should be modified.

For ACC output, referring to (A20), $\Delta\mathbf{M_{dq}}$ can be obtained:

$$\begin{aligned}\Delta\mathbf{M_{dq}} &= \mathbf{G_{Mdquxy}}\Delta\mathbf{u_{pxy}} + \mathbf{G_{Mdqixy}}\Delta\mathbf{i_{xy}} + \\ &\left(\begin{bmatrix} G_{in}G_{out} \\ 0 \end{bmatrix}D_{uc}\left[\mathbf{0}_{1\times4}\ 1\right]\right)_{\mathbf{G_{Mdquc}}}\Delta\mathbf{u_c^{\Sigma}}\end{aligned} \tag{A40}$$

where D_{uc} is the transfer function for signal filter of the average capacitor voltage. Similar to (A28), $\Delta\mathbf{M_{xy}}$ can be further expressed as:

$$\Delta\mathbf{M_{xy}} = \mathbf{G_{Mxyu}}\Delta\mathbf{u_{pxy}} + \mathbf{G_{Mxyi}}\Delta\mathbf{i_{xy}} + \left(\mathbf{C_{03}G_{Mdquc}}\right)_{\mathbf{G_{Mxyuc}}}\Delta\mathbf{u_c^{\Sigma}} \tag{A41}$$

The small-signal model of DCC output is:

$$\begin{aligned}\Delta M_{dc} &= \left[\left(K_{Udcs} - G_{dcin}G_{dcout}\right)D_{udc}\right]_{G_{Mdcudc}}\Delta u_{dc} + \\ &\left(-3G_{dcin}D_{idc}\right)_{G_{Mdci0}}\Delta i_{diff\,0}\end{aligned} \tag{A42}$$

where $G_{dcin} = K_{PIdc} + K_{IIdc}/s$, $G_{dcout} = K_{POdc} + K_{IOdc}/s$. D_{udc} and D_{idc} are the transfer functions of signal filters for the DC voltage and DC current.

Referring to (A34), the group of algebra equations should be modified as (A43). The difference between (A34) and (A43) is highlighted.

$$\begin{bmatrix} \mathbf{G_i} & \mathbf{G_{evuc}} & \mathbf{0_{2*2}} & \mathbf{G_{evM}} & \mathbf{G_{evM2}} & \mathbf{0_{2*1}} & \mathbf{0_{2*1}} & \mathbf{G_{evMdc}} \\ \mathbf{G_{uci}} & \mathbf{-G_{uc}} & \mathbf{G_{ucidiff}} & \mathbf{G_{ucM}} & \mathbf{G_{ucM2}} & \mathbf{G_{uci0}} & \mathbf{0_{5*1}} & \mathbf{G_{ucMdc}} \\ \mathbf{0_{2*2}} & \mathbf{G_{idiffuc}} & \mathbf{-G_{idiff}} & \mathbf{G_{idiffM}} & \mathbf{G_{idiffM2}} & \mathbf{0_{2*1}} & \mathbf{0_{2*1}} & \mathbf{G_{idiffMdc}} \\ \mathbf{G_{Mxyi}} & \mathbf{G_{Mxyuc}} & \mathbf{0_{2*2}} & \mathbf{-I_{2*2}} & \mathbf{0_{2*2}} & \mathbf{0_{2*1}} & \mathbf{0_{2*1}} & \mathbf{0_{2*1}} \\ \mathbf{0_{2*2}} & \mathbf{0_{2*5}} & \mathbf{G_{Mxy2i2}} & \mathbf{0_{2*2}} & \mathbf{-I_{2*2}} & \mathbf{0_{2*1}} & \mathbf{0_{2*1}} & \mathbf{0_{2*1}} \\ \mathbf{0_{1*2}} & \mathbf{G_{i0uc}} & \mathbf{0_{1*2}} & \mathbf{G_{i0M}} & \mathbf{G_{i0M2}} & \mathbf{-G_{i0}} & \mathbf{G_{i0udc}} & \mathbf{G_{i0Mdc}} \\ \mathbf{0_{1*2}} & \mathbf{0_{1*5}} & \mathbf{0_{1*2}} & \mathbf{0_{1*2}} & \mathbf{0_{1*2}} & 3u_{dc0} & i_{dc0} & 0 \\ \mathbf{0_{1*2}} & \mathbf{0_{1*5}} & \mathbf{0_{1*2}} & \mathbf{0_{1*2}} & \mathbf{0_{1*2}} & G_{Mdci0} & G_{Mdcudc} & -1 \end{bmatrix}_{\mathbf{G_{ii}}} \cdot \begin{bmatrix} \Delta\mathbf{i_{xy}} \\ \Delta\mathbf{u_c^{\Sigma}} \\ \Delta\mathbf{i_{diffxy2}} \\ \Delta\mathbf{M_{xy}} \\ \Delta\mathbf{M_{xy2}} \\ \Delta i_{diff\,0} \\ \Delta u_{dc} \\ \Delta M_{dc} \end{bmatrix} = \begin{bmatrix} \mathbf{I_{2*2}}/K_T \\ \mathbf{0_{5*2}} \\ \mathbf{0_{2*2}} \\ \mathbf{-G_{Mxyu}} \\ \mathbf{-G_{Mxy2u}} \\ \mathbf{0_{1*2}} \\ \mathbf{0_{1*2}} \\ \mathbf{0_{1*2}} \end{bmatrix}_{\mathbf{G_{uu}}}\Delta\mathbf{u_{pxy}} \tag{A43}$$

The expression of the AC impedance for the HY-MMC is the same as (A35).

TABLE AI
PARAMETERS OF THE TESTED SYSTEM

Half-bridge /Hybrid MMC	Rated DC voltage	640kV
	Rated capacity	1000MW
	Arm inductance	112mH
	Arm equivalent resistance	0.01Ω
	Number of FBSM/HBSM (HY-MMC)	100/100
	Number of HBSM (HB-MMC)	200
	Submodule capacitance	10 mF
Two-level VSC	Rated DC voltage	640kV
	Rated capacity	1000MW
	DC capacitance	0.3mF
AC transformer	Rated voltage grid/converter-side	400kV/352kV
	Leak inductance	15%
AC system	Rated voltage	400 kV
	Impedance (AC system 1, SCR=2)	$80\angle85.62°\Omega$
	Impedance (AC system 2, SCR=20)	$8\angle82.83°\ \Omega$

TABLE AII
CONTROL PARAMETERS OF THE CONVERTERS

	Control parameters	VSCs
PLL	K_{Ppll}	80

	K_{IpII}	500
ACC	K_{PO}	1(*Inv.*) 0.4 (*Rec.*)
	K_{IO}	100(*Inv.*) 300 (*Rec.*)
	K_{PI}	1
	K_{II}	50
DCC (for HY-MMC only)	K_{POdc}	1.2
	K_{IOdc}	800
	K_{PIdc}	2
	K_{IIdc}	100
	K_{Udcs}	1
Cutting-off frequencies for second-order low-pass signal filters	active/reactive power	800Hz
	AC voltage	300Hz
	AC current	800Hz
	DC voltage	300Hz
	DC current	800Hz
	Sub-module capacitor voltage	500Hz

REFERENCES

[1] N. Flourentzou, V. G. Agelidis and G. D. Demetriades, "VSC-Based HVDC Power Transmission Systems: An Overview," *IEEE Trans. Power Electron.*, vol. 24, no. 3, pp. 592-602, March 2009.

[2] A. Lesnicar and R. Marquardt, "An innovative modular multilevel converter topology suitable for a wide power range," *Proc. IEEE Power Tech Conf.*,, Bologna, Italy, 2003, pp. 1-6

[3] R. Zeng, L. Xu, L. Yao and B. W. Williams, "Design and Operation of a Hybrid Modular Multilevel Converter," *IEEE Trans. Power Electron.*, vol. 30, no. 3, pp. 1137-1146, March 2015.

[4] S. Yang, W. Xiang, R. Li, et al., "An Improved DC fault Protection Algorithm for MMC HVDC Grids based on Modal Domain Analysis," *IEEE J. Emerg. Sel. Top. Power Electron.*, early access, to be published.

[5] W. Xiang, S. Yang, L. Xu, et al., "A Transient Voltage based DC Fault Line Protection Scheme for MMC based DC Grid Embedding DC Breakers," *IEEE Trans. Power Del*, vol. 34, no. 1, pp. 334-345, Feb. 2019.

[6] W. Lin, D. Jovcic, S. Nguefeu and H. Saad, "Full-Bridge MMC Converter Optimal Design to HVDC Operational Requirements," *IEEE Trans. Power Del.*, vol. 31, no. 3, pp. 1342-1350, June 2016.

[7] W. Xiang, W. Lin, L. Xu and J. Wen, "Enhanced Independent Pole Control of Hybrid MMC-HVdc System," *IEEE Trans. Power Del.*, vol. 33, no. 2, pp. 861-872, April 2018.

[8] Y. Huang, X. Yuan, J. Hu, P. Zhou and D. Wang, "DC-Bus Voltage Control Stability Affected by AC-Bus Voltage Control in VSCs Connected to Weak AC Grids," *IEEE J. Emerg. Sel. Top. Power Electron.*, vol. 4, no. 2, pp. 445-458, June 2016.

[9] D. Wang, L. Liang, L. Shi, J. Hu and Y. Hou, "Analysis of Modal Resonance Between PLL and DC-Link Voltage Control in Weak-Grid Tied VSCs," *IEEE Trans. Power Syst.*, vol. 34, no. 2, pp. 1127-1138, March 2019.

[10] J. Khazaei, M. Beza and M. Bongiorno, "Impedance Analysis of Modular Multi-Level Converters Connected to Weak AC Grids," *IEEE Trans. Power Syst.*, vol. 33, no. 4, pp. 4015-4025, July 2018.

[11] B. Wen, D. Boroyevich, R. Burgos, P. Mattavelli and Z. Shen, "Small-Signal Stability Analysis of Three-Phase AC Systems in the Presence of Constant Power Loads Based on Measured d-q Frame Impedances," *IEEE Trans. Power Electron.*, vol. 30, no. 10, pp. 5952-5963, Oct. 2015.

[12] B. Wen, D. Boroyevich, R. Burgos, P. Mattavelli and Z. Shen, "Analysis of D-Q Small-Signal Impedance of Grid-Tied Inverters," *IEEE Trans. Power Electron*, vol. 31, no. 1, pp. 675-687, Jan. 2016.

[13] B. Wen, D. Dong, D. Boroyevich, R. and et al., "Impedance-Based Analysis of Grid-Synchronization Stability for Three-Phase Paralleled Converters," *IEEE Trans. Power Electron*, vol. 31, no. 1, pp. 26-38, Jan. 2016.

[14] Y. Li, G. Tang, T. An, and et al., "Power Compensation Control for Interconnection of Weak Power Systems by VSC-HVDC," *IEEE Trans. Power Del.*, vol. 32, no. 4, pp. 1964-1974, Aug. 2017.

[15] C. Zou, H. Rao, S. Xu, et al., "Analysis of Resonance Between a VSC-HVDC Converter and the AC Grid," *IEEE Trans. Power Electron.*, vol. 33, no. 12, pp. 10157-10168, Dec. 2018.

[16] X. Lu, W. Xiang and J. Wen, "Enhancing Active Power Transfer Capability for Hybrid MMC Integrated with Weak AC Grid through Parameter Adjustment," *Proc. 45th Annu. Conf. IEEE Ind. Electron. Soc.*, Lisbon, Portugal, 2019, pp. 4805-4810.

[17] J. Beerten, G. B. Diaz, S. D'Arco and J. A. Suul, "Comparison of small-signal dynamics in MMC and two-level VSC HVDC transmission schemes," in *Proc. IEEE Int. Energy Conf.*, Leuven, 2016, pp. 1-6.

[18] X. Lu, W. Xiang, W. Lin, J. Wen. "State-space model and PQ operation zone analysis of hybrid MMC," *Electr. Power Syst. Res.*, vol. 162, pp. 99-108, September 2018.

[19] X. Lu, W. Xiang, W. Lin, J. Wen, "Small-signal modeling of MMC based DC grid and analysis of the impact of DC reactors on the small-signal stability," *Int. J. Electr. Power Energy Syst.* vol. 101, pp. 25-37, October 2018.

[20] A. Jamshidifar and D. Jovcic, "Small-Signal Dynamic DQ Model of Modular Multilevel Converter for System Studies," *IEEE Trans. Power Del.*, vol. 31, no. 1, pp. 191-199, Feb. 2016.

[21] J. Freytes *et al.*, "Improving Small-Signal Stability of an MMC With CCSC by Control of the Internally Stored Energy," *IEEE Trans. Power Del.*, vol. 33, no. 1, pp. 429-439, Feb. 2018.

[22] P. Kundur. "Power System Stability and Control," *McGraw-Hill*, 1994.

[23] S. Shah and L. Parsa, "Impedance Modeling of Three-Phase Voltage Source Converters in DQ, Sequence, and Phasor Domains," *IEEE Trans. Energy Convers.*, vol. 32, no. 3, pp. 1139-1150, Sept. 2017.

[24] J. Z. Zhou, A. M. Gole. "Rationalisation and validation of dc power transfer limits for voltage sourced converter based high voltage DC transmission", *IET Gener. Transm. Distrib.*, vol. 10, no. 6, pp. 1327–1335, May, 2016.

[25] G. Wu et al., "Analysis and design of vector control for VSC-HVDC connected to weak grids," *CSEE J. Power Energy Syst.*, vol. 3, no. 2, pp. 115-124, June 2017.

[26] M. F. M. Arani and Y. A. I. Mohamed, "Analysis and Performance Enhancement of Vector-Controlled VSC in HVDC Links Connected to Very Weak Grids," *IEEE Trans. Power Syst.*, vol. 32, no. 1, pp. 684-693, Jan. 2017.

[27] Y. Huang and D. Wang, "Effect of Control-Loops Interactions on Power Stability Limits of VSC Integrated to AC System," *IEEE Trans. Power Del.*, vol. 33, no. 1, pp. 301-310, Feb. 2018.

[28] A. J. Agbemuko, J. L. Dominguez-Garcia, O. Gomis-Bellmunt and L. Harnefors, "Passivity-Based Analysis and Performance Enhancement of a Vector Controlled VSC Connected to a Weak AC Grid," *IEEE Trans Power Del.* Early access, to be published.

BIOGRAPHIES

Xiaojun Lu received his B.Eng. and PhD degrees both in electrical engineering from Huazhong University of Science and Technology (HUST), China in 2013 and 2018, respectively. Currently, he is a postdoctor with HUST since 2018. His main research interests include modeling and stability analysis of MMC-HVDC and dc grids.

Wang Xiang (S'16-M'17) received his B.Eng. and PhD degrees both in electrical engineering from Huazhong University of Science and Technology (HUST), China in 2012 and 2017, respectively. He was a visiting student at the University of Aberdeen and the University of Strathclyde in 2014 and 2016 respectively. Currently, he is a research associate with the University of Strathclyde since 2018. His main research interests include MMC-HVDC, high power dc/dc converters and dc grids.

Weixing Lin (M'13) obtained his B.E. and PhD degrees in electrical engineering from Huazhong University of Science and Technology (HUST), China, in 2008 and 2014 respectively. He was a research fellow at University of Aberdeen during 2012-2016. He is currently the chief engineer of HVDC division at TBEA China Xinjiang *Sunoasis* Co. Ltd. His research interests are HVDC, MMC, dc-dc autotransformer, DC grids.

Jinyu Wen (M'10) received his B.Eng. and Ph.D. degrees all in electrical engineering from Huazhong University of Science and Technology (HUST), Wuhan, China, in 1992 and 1998, respectively. He was a visiting student from 1996 to 1997 and a research fellow from 2002 to 2003 all at the University of Liverpool, UK, and a senior visiting researcher at the University of Texas at Arlington, USA in 2010. From 1998 to 2002 he was a director engineer in XJ Electric Co. Ltd. in China. In 2003 he joined the HUST and now is a Professor at HUST. His current research interests include renewable energy integration, energy storage application, DC grid, and power system operation and control.